



AD-A282 524



NRL/FR/7210--94-9727

①

# Millimeter-Wave Radiometric Utility Study

JAMES P. HOLLINGER  
STEVEN R. HIGHLEY  
GLENN D. SANDLIN, EDITOR

**S** DTIC  
ELECTE  
JUL 27 1994  
**F**

*RadiolIR/Optical Sensors Branch  
Remote Sensing Division*

June 22, 1994

"Original contains color  
plates: All DTIC reproduct-  
ions will be in black and  
white"

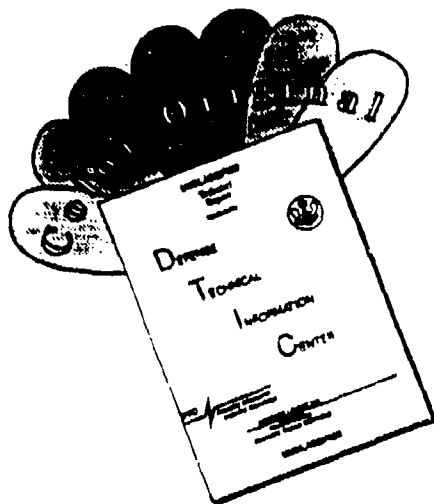
copy 94-23441



Approved for public release; distribution unlimited.

94 7 25 079

# DISCLAIMER NOTICE



THIS DOCUMENT IS BEST QUALITY AVAILABLE. THE COPY FURNISHED TO DTIC CONTAINED A SIGNIFICANT NUMBER OF COLOR PAGES WHICH DO NOT REPRODUCE LEGIBLY ON BLACK AND WHITE MICROFICHE.

# REPORT DOCUMENTATION PAGE

*Form Approved*  
OMB No. 0704-0188

Public reporting burden for this collection of information is estimated to average 1 hour per response, including the time for reviewing instructions, searching existing data sources, gathering and maintaining the data needed, and completing and reviewing the collection of information. Send comments regarding this burden estimate or any other aspect of this collection of information, including suggestions for reducing this burden, to Washington Headquarters Services, Directorate for Information Operations and Reports, 1215 Jefferson Davis Highway, Suite 1204, Arlington, VA 22202-4302, and to the Office of Management and Budget, Paperwork Reduction Project (0704-0188), Washington, DC 20503.

1. AGENCY USE ONLY (Leave Blank)	2. REPORT DATE  June 22, 1994	3. REPORT TYPE AND DATES COVERED  Oct. 1991 - July 1993	
4. TITLE AND SUBTITLE  Millimeter-Wave Radiometric Utility Study		5. FUNDING NUMBERS  WU - PMW-165 -NRL-94-3(X1506)	
6. AUTHOR(S)  James P. Hollinger, Steven R. Highley, and Glenn D. Sandlin (editor)			
7. PERFORMING ORGANIZATION NAME(S) AND ADDRESS(ES)  Naval Research Laboratory Washington, DC 20375-5320		8. PERFORMING ORGANIZATION REPORT NUMBER  NRL/FR/7210-94-9727	
9. SPONSORING/MONITORING AGENCY NAME(S) AND ADDRESS(ES)		10. SPONSORING/MONITORING AGENCY REPORT NUMBER	
11. SUPPLEMENTARY NOTES			
12a. DISTRIBUTION/AVAILABILITY STATEMENT  Approved for public release; distribution unlimited.		12b. DISTRIBUTION CODE	
13. ABSTRACT (Maximum 200 words)  The purpose of this task is two-fold. The general purpose is to provide an introductory discussion of passive millimeter-wave radiometry and its value to remote sensing, illustrated by examples of imagery. The imagery of relatively high resolution has been acquired at various frequencies from aircraft, and the imagery of lower resolution (12.5 km), also important in intelligence gathering, has been acquired by the 85.5 GHz channel of the DMSP-SSM/I (F8). Examples of military, man-made, and environmental targets illustrate the all-weather capability of passive millimeter-wave systems and the types of signatures received. The meteorological subjects—particularly the millimeter-wave characteristics of tropical cyclones, frontal systems, and clouds—have become the basis of additional environmental work at NRL (to be published later under separate cover). The more specific purpose in this report is to study the utility of passive millimeter-wave imaging from space enhanced with systems that provide surface resolutions of 100-400 m and operate at 90 GHz. The utility, including limitations, of this system for target detection, surveillance, and environmental monitoring is discussed.			
14. SUBJECT TERMS  Millimeter-wave radiometry All-weather capability Environmental monitoring		Surveillance DMSP-SSM/I	15. NUMBER OF PAGES  71
17. SECURITY CLASSIFICATION OF REPORT  UNCLASSIFIED		18. SECURITY CLASSIFICATION OF THIS PAGE  UNCLASSIFIED	16. PRICE CODE
19. SECURITY CLASSIFICATION OF ABSTRACT  UNCLASSIFIED		20. LIMITATION OF ABSTRACT  UL	

## CONTENTS

INTRODUCTION .....	1
MILLIMETER-WAVE RADIOMETRY .....	1
Brightness Temperature .....	1
Antenna Temperature .....	2
Receiver Noise Temperature .....	2
Minimum Detectable Signal .....	3
Target Contrast .....	3
BASELINE INSTRUMENT .....	5
Orbit Description .....	5
Baseline Instrument Design .....	8
Technology .....	15
Tradeoffs .....	16
TARGET/BACKGROUND CHARACTERISTICS .....	16
Millimeter-wave Image Characteristics .....	16
Clutter .....	16
Atmospheric Temporal Variations .....	25
Military Targets .....	25
Aircraft, Tanks, and Vehicles .....	25
Ships and Ship Wakes .....	33
Infrastructure .....	36
Battlefield Damage Assessment .....	36
Environmental Signatures .....	38
Surface Signatures .....	38
Oil Spills .....	38
Atmospheric Signatures .....	52
Operation Desert Storm .....	61
SUMMARY .....	66
REFERENCES .....	66

□
□
□

Distribution /	
Availability Codes	
Dist	Avail and/or Special
A-1	

## MILLIMETER-WAVE RADIOMETRIC UTILITY STUDY

### INTRODUCTION

Wide-area surveillance on a timely and global basis is critical for many military and environmental applications. Passive millimeter-wave imaging has the advantage over visual and infrared systems of being a near-all-weather surveillance system with the ability to see through ninety percent of all clouds and most adverse weather conditions, with equal day time and night time sensitivity. The major drawback of millimeter-wave radiometric systems is that the relatively long wavelengths require very large apertures, several orders of magnitude larger than at infrared, to obtain similar high resolution. However even "low" resolution millimeter-wave systems may contribute significantly to intelligence gathering and environmental monitoring.

The purpose of this task is two-fold. The general purpose is to provide an introductory discussion of passive millimeter-wave radiometry and its value to remote sensing, illustrated by examples of imagery. The imagery of relatively high resolution has been acquired at various frequencies from aircraft or truck, and the imagery of lower resolution (12.5 km), also important in intelligence gathering, has been acquired by the 85.5 GHz channel of the DMSP-SSM/I (F8). Examples of military, man-made, and environmental targets illustrate the all-weather capability of passive millimeter-wave systems and the types of signatures received. The meteorological subjects observed with the SSM/I, particularly the millimeter-wave characteristics of tropical cyclones, frontal systems, and clouds have become the basis of additional environmental work with the SSM/I (to be published later under separate cover).

The more specific purpose of this task is to study the utility of passive millimeter-wave imaging from space with systems that provide surface resolutions of 100 to 400 m. A baseline design for a low-resolution multiple real-beam imaging system, operating at 90 GHz and designed around existing technology, is used to explore various applications and predict the usefulness of this technology. Both a low Earth circular polar orbit at 400 km and an elliptical orbit at 60-deg inclination with a perigee of 400 km and apogee of 1000 km are considered. The resulting swath width, search rate, resolution, and integration time are used to estimate signal-to-noise ratios for a wide range of man-made and environmental targets for various atmospheric conditions. The utility of this system for target detection, surveillance, and environmental monitoring is discussed.

### MILLIMETER-WAVE RADIOMETRY

#### Brightness Temperature

The power received by an Earth-viewing radiometer consists of man-made radiations from point sources and the self or blackbody type radiation from targets and the background environment. The millimeter-wave signal is composed of three types of radiation:

Manuscript received September 7, 1993.

- that emitted by targets and the Earth's surface,
- the downwelling radiation emitted by the atmosphere and then reflected by the surface, and
- the upward emission and attenuation of the atmosphere between the surface and the radiometer.

The intensity of radiation, in watts/M<sup>2</sup>/Hz/steradian, from a blackbody at a physical temperature  $T$  is given by Planck's Law as

$$I = (h\nu/\lambda^2)/[\exp(h\nu/KT) - 1], \quad (1)$$

where  $h$  and  $K$  are Planck's and Boltzmann's constants respectively,  $\nu$  is the frequency, and  $\lambda$  is the wavelength. At millimeter-wave frequencies, where  $KT \gg h\nu$ , the Rayleigh-Jeans approximation to the Planck blackbody radiation law applies and

$$I \cong KT/\lambda^2 \quad (2)$$

Therefore the power radiated by a perfectly radiating surface per unit bandwidth is proportional to the physical temperature  $T$  of the material. If the surface is not a perfect radiator but has an emissivity  $e$  of  $< 1$ , the power radiated is proportional to  $eT$ . Even if the source is man-made and radiates by some nonthermal process, the power it radiates can be specified by a temperature. This temperature is the physical temperature a blackbody radiator must have to radiate the same power as the nonthermal source over the same bandwidth. Thus the power radiated from any target and the environmental background can be specified by a brightness temperature. This equivalent brightness temperature  $T_b$  can easily be millions of degrees for nonthermal sources.

### Antenna Temperature

It is convenient to also specify by temperature the power received by the antenna and delivered to the receiver input. This is possible because of the Nyquist's theorem, which states that the power available at the terminals of a resistor per unit bandwidth is proportional to the physical temperature of the resistor. Thus an antenna temperature  $T_A$  can be defined as the temperature of an impedance, identical to the antenna impedance, which when connected in place of the antenna delivers the same power to the receiver as does the antenna. A millimeter-wave radiometer measures the absolute level of the total power received by its antenna at a particular polarization over its reception bandwidth. In general, high-gain antennas receive power primarily over a relatively narrow beam or solid angle; however some power is usually received from all directions. The power received in these sidelobes and backlobes, although small, is normally not desired and a correction is applied to remove it. The antenna temperature is the average of the brightness temperature over all directions, weighted by the antenna gain  $G$ :

$$T_A(r,t) = \int T_B(r,t) G(r - r') d\Omega/4\pi \quad (3)$$

This power is then amplified by the receiver and appears at the receiver output terminals.

### Receiver Noise Temperature

In any realizable receiver, random noise is generated by the receiver in the amplification of the desired signal and unavoidably appears with it at the output terminals. This situation may be equally well

represented by the addition of an unwanted noise power to the input signal at the input terminals of an ideal noiseless receiver, which is then amplified along with the desired signal. This noise power may also be specified by a temperature  $T_N$ . This is the temperature to which the input impedance of the receiver must be raised in order that, when amplified by the ideal noiseless receiver, the noise power, per unit bandwidth, at the output terminals is identical to the noise generated by the real receiver. The receiver noise power  $T_N$  is essentially "white" noise with a flat power spectrum extending far beyond the spectrum of  $T_A$ . It is therefore necessary to filter or remove the receiver noise contribution at equivalent spatial frequencies where there is no signal from the antenna. The signal measured at the output of the receiver is

$$T_M(t) = \int [T_A(r, t') + T_N(t')] H(t - t') dt' \quad (4)$$

where  $H$  is the impulse response of the receiver low-pass filter. The dwell or integration time  $\tau$  on the scene is determined by the cutoff frequency of the low-pass filter,  $\Delta f_c$ . For an ideal low-pass filter  $\tau = 1/(2\Delta f_c)$ .

### Minimum Detectable Signal

The minimum detectable signal  $\Delta T_N$  is given by

$$\Delta T_N = K_{sys} T_{sys} [\Delta f \tau]^{-1/2} \quad (5)$$

where  $T_{sys}$  includes both the receiver noise  $T_N$  and the signal from the antenna  $T_A$ ;  $K_{sys}$  is a sensitivity constant of order unity and depends on the type of receiver; and  $\Delta f$  is the predetection bandwidth of the receiver.

Therefore it is possible to describe the signal from the target and background in terms of a brightness temperature, the signal received by the antenna as an antenna temperature, and the quality of the receiver as a noise temperature. Note that  $T_B$  is an inherent property of the scene being viewed while both  $T_A$  and  $T_N$  can be selected to some degree by the design of the antenna and receiver.

### Target Contrast

The effective antenna beam solid angle  $\Omega_e$  is defined as the solid angle through which all the power from a transmitting antenna would flow if the power were constant over this angle and equal to the peak value. It is given by

$$\Omega_e = \int_{r\pi} [G(r)/G_0] d\Omega = 4\pi/G_0, \quad (6)$$

where  $G(r)$  is the antenna gain in direction  $r$ , and  $G_0$  is the peak gain. The main beam solid angle  $\Omega_B$  is defined similarly, but with the restriction that the power is now just that from the main lobe up to the first null—not the entire power pattern. The ratio  $\Omega_B/\Omega_e$  is the main beam efficiency and is typically  $\sim 0.9$  for filled apertures. The solid angle subtended by a target  $\Omega_t$  is determined by limiting the integral of Eq. (6) to those directions from which power is received from the target.

The target contrast  $\Delta T_A$  is defined as the difference between the antenna temperature when a target is present in the antenna beam and when it is not. Following Eq. (3) the target contrast is given by

$$\Delta T_A = T_{At} - T_{Ab} = \int_{4\pi} T_{Bt} G d\Omega / 4\pi - \int_{4\pi} T_{Bb} G d\Omega / 4\pi \quad (7)$$

where  $T_{Bt}$  and  $T_{Bb}$  are the scene brightness temperatures when the target is present and when it is not, respectively. Equation (7) may be rewritten by using the definitions of Eq. (6) as

$$\Delta T_A = [\Omega_t / \Omega_e] \int_t (T_{Bt} - T_{Bb} - T_{Bb}) G d\Omega / \int_t G d\Omega . \quad (8)$$

Thus the target contrast is the normalized integral over the solid angle subtended by the target of the brightness temperature difference between the target and background, weighted by the antenna gain and reduced by the ratio of the target solid angle to the effective beam solid angle. Note that  $\Omega_t / \Omega_e$  is approximately equal to  $A_t / 2A_{BW}$ .  $A_t$  is the target, and  $A_{BW}$  is the half-power beam-width on Earth's surface. Therefore for targets smaller than the half-power beamwidth

$$\Delta T_A \cong (A_t / 2A_{BW}) (T_{Bt} - T_{Bb}). \quad (9)$$

For targets large compared to the half-power beamwidth  $\Omega_t$  is approximately equal to  $\Omega$ , and  $\Delta T_A = [T_{Bt} - T_{Bb}]$ .

As described above, the millimeter-wave radiometric signal is composed of not only the radiation emitted by the target and background, but also of the downwelling radiation emitted by the atmosphere reflected by the surface, as well as the upward emission and attenuation of the atmosphere between the surface and the radiometer. The brightness temperature contributing to  $\Delta T_A$  as seen by a radiometer looking at Earth from space can be written as

$$T_{Bb} = e_b T_0 (1 - \alpha) + (1 - e_b) \alpha T_0 (1 - \alpha) + \alpha T_0 . \quad (10)$$

Here  $\alpha$  is the fractional atmospheric loss and  $e_b$  is the emissivity of the background;  $(1 - e_b)$  is then the reflectivity of the background. The physical temperatures of the atmosphere and background are assumed to be equal and are given by  $T_0$ . In this case, the atmospheric radiation is specified by  $\alpha T_0$ . The first term in Eq. (10) represents the radiation emitted by Earth,  $e_b T_0$ , attenuated by the atmosphere  $(1 - \alpha)$ . The second term arises from the downwelling atmospheric radiation,  $\alpha T_0$  reflected from Earth's surface  $(1 - e_b)$ , and attenuated by the atmosphere,  $(1 - \alpha)$ . The last term represents the upwelling atmospheric radiation. Equation (10) can be rewritten as

$$T_{Bb} = e_b T_0 (1 - \alpha)^2 + \alpha T_0 (2 - \alpha). \quad (11)$$

Similarly, the radiation received from the target is given by

$$T_{Bb} = e_t \delta T (1 - \alpha) + e_b T_0 (1 - \alpha)^2 + \alpha T_0 (2 - \alpha), \quad (12)$$

where  $\delta T$  is the difference in the physical temperature, if any, between the target and the background and  $e_t$  is the emissivity of the target. The contrast is then from Eqs. (9), (11), and (12):

$$\Delta T_A = \left( \frac{A_t}{2A_{BW}} \right) [e_t \delta T (1 - \alpha) + (e_t - e_b) T_0 (1 - \alpha)^2] \quad (13)$$

Note that:

- the larger the target, the greater the signal until the antenna beam is filled'
- the greater the difference in emissivities, the greater the signal;
- the larger the atmospheric losses, the smaller the signal;
- with the right combination of  $\delta T$ ,  $e_t - e_b$ , and  $\alpha$ , the target can disappear; and
- signals can be positive or negative.

The signal-to-noise S/N of the target is given by the ratio of Eqs. (13) and (5):

$$S/N = \frac{\left( \frac{A_t}{2A_{BW}} \right) [e_t \delta T (1 - \alpha) + (e_t - e_b) T_0 (1 - \alpha)^2]}{[K_{sys} T_{sys} (\Delta f \tau)^{-1/2}]} \quad (14)$$

The target is defined by its area  $A_t$ , its emissivity  $e_t$ , and physical temperature  $T_0$ ; and temperature difference from the background  $\delta T$ . The weather is specified by the atmospheric loss  $\alpha$  and the background by its emissivity  $e_b$ . The radiometric system is defined by  $K_{sys}$ ,  $T_{sys}$ ,  $\Delta f$ , and  $A_{BW}$ . The orbit is specified by the dwell time  $\tau$  and  $A_{BW}$ . It should be noted that while the physical temperature difference between the target and background,  $\delta T$ , is the primary contributor to scene contrast at infrared, it is generally negligible compared to the emissivity difference between the target and background,  $(e_t - e_b)$ , at millimeter-wave frequencies. In most cases, the term  $e_t \delta T (1 - \alpha)$  may be set to 0 in Eq. (14). With clear skies and low humidity,  $\alpha$  is near 0. With rain or heavy clouds,  $\alpha$  will increase to near 1. Table 1 gives typical values of  $\alpha$  at 90 GHz for polar, temperate and tropical climates, with and without clouds present. Table 2 gives representative values of  $\alpha$  for various atmospheric constituents. The emissivity  $e_t$  will vary from near 0 for a metal surface to 1 for absorbing material. Emissivity  $e_b$  for the sea surface is about 0.6 at 90 GHz and varies between about 0.7 and 0.9 for land, depending largely on the moisture content of the soil. Tables 3-5 give emissivity values at 90 GHz, for various targets and environmental features.

## BASELINE INSTRUMENT

### Orbit Description

Two orbits are considered for the baseline system, a 400-km circular, near-polar orbit and a 60-deg-inclined elliptical orbit with 1000-km apogee and 400-km perigee. For an extended satellite lifetime, the altitude must be high enough to avoid atmospheric drag (300 to 400 km minimum). The 400-km polar orbit will provide a lifetime of several years and allows total Earth coverage. The varying altitude of an elliptical orbit causes the resolution to vary throughout the orbit, but it gives a shorter revisit time for the area of Earth that the orbit covers. Highly elliptical orbits with the perigee between 100 and 200 km

Table 1 -- Average Atmospheric Loss at 90 GHz

Climate	Loss in dB		Fractional loss $\alpha$	
	Clear	Cloudy	Clear	Cloudy
<b>Tropical</b>				
Winter	2.0	4.8	0.38	0.67
Spring	2.6	6.0	0.45	0.75
Summer	2.9	6.2	0.49	0.76
Autumn	2.6	5.2	0.45	0.70
<b>Temperate</b>				
Winter	0.8	2.8	0.16	0.48
Spring	1.0	2.8	0.21	0.48
Summer	1.4	3.2	0.27	0.52
Autumn	1.1	3.6	0.22	0.56
<b>Polar</b>				
Winter	0.5	2.6	0.10	0.46
Spring	0.5	1.6	0.12	0.32
Summer	0.7	2.3	0.15	0.41
Autumn	0.5	4.1	0.10	0.62

Table 2 -- Characteristics of Weather Targets at 90 GHz

Target	Area (m <sup>2</sup> )	Emissivity	Temperature (K)
Low rain rates over ocean	Beam fill	0.9	280
High rain rates over ocean	Beam fill	0.5	280
Tropical storms	Beam fill	0.2 - 0.9	270
Tornados	8000	0.2 - 0.9	270
Squall lines	Beam fill	0.5 - 0.9	275
Fronts	Beam fill	0.6 - 0.9	275
Dust storms	Beam fill	0.9	300
Cloud cover	Beam fill	<0.9	260
Convergent winds	Beam fill	0.6	286

Table 3 — Percentage Contributions of Atmospheric Constituents to the Upwelling Radiation from a Thunderstorm

Constituent	Thunderstorm			Clear Sky
	Front	Core	Rear	
Cloud drops	38.2	46.6	49.9	0.0
Rain drops	54.1	16.7	19.9	0.0
Graupel particles	0.2	17.9	4.9	0.0
Ice crystals	0.1	11.3	14.9	0.0
Aggregates	0.0	0.1	1.1	0.0
Gases	6.0	7.0	9.1	11.0
Earth's surface	1.4	0.0	0.1	88.0
Cosmic background	0.1	0.3	0.1	0.0

Table 4 — Characteristics of Environmental Targets at 90 GHz

Target	Area (m <sup>2</sup> )	Emissivity	Temperature (K)
Oil spill	Beam fill	0.6	286
Fires	10000	0.95 - 1.0	700
Vegetation	10000	0.9	300
Soil moisture	2500	0.7	300
Snow cover	Beam fill	0.8	270
Ice	Beam fill	0.7 - 0.9	270
Pollution	2500	0.91 - 0.93	300
Vegetation stress	10000	0.87	300
Slash and burn	40000	0.7	300
Rivers	2500	0.6 - 0.7	300
Icebergs	5000	0.7	268

Table 5 — Environmental Loss at 90 GHz

Environment	Loss in dB	Fractional loss $\alpha$
Clear sky	1	0.21
Dry air	0.04/km	0.009/km
Moist air	0.4/km	0.088/km
Humid air	2/km	0.37/km
Fog	1.5/km	0.27/km
Clouds	5/km	0.68/km
Ice clouds	$\approx 0$ /km	$\approx 0$ /km
Light rain	1 - 3/km	0.2 - 0.99/km
Heavy rain	10 - 20/km	0.90 - 0.99/km
Tropical storm	> 30/km	> 0.999
Snow storm	10/km	0.9/km
Light smoke	$\approx 0$ /km	$\approx 0$ /km
Heavy smoke	$\approx 0$ /km	$\approx 0$ /km
Dust	$\approx 2$ /km	0.4/km
Chemicals	?	?
Vegetation	1/LAI	0.21/LAI
Earth	20/cm	0.99/cm
Sand	2/cm	0.37/cm

would increase resolution for a short time while maintaining a reasonable satellite lifetime. Integration time is selected as the time for the beam to move half a beamwidth. Since the speed of the ground track is inversely related to the altitude, higher altitudes give lower speeds. Altitude will govern integration time and hence the receiver's rms noise level. Because varying integration times would unnecessarily complicate data processing, the integration time for the elliptical orbit is derived by the speed at perigee and held constant for the entire orbit. Table 6 compares system characteristics for three sizes of antennas and two orbits. Revisit times will vary not only with altitude but also with the latitude of the scene (Fig. 1) for a polar orbit. The actual orbit can be designed to produce one of many different ground tracks, depending on program requirements.

### Baseline Instrument Design

The baseline instrument is designed to have 100- to 400-m resolution from a reasonable orbit and use present or near-term components. The resolution on the ground  $dx$  is the altitude  $h$  times the antenna beamwidth  $BW$ ,  $dx = h BW$ , where  $BW = k \lambda/D$ ;  $D$  being the aperture diameter,  $\lambda$  the wavelength, and  $k$  a constant related to the field distribution over the aperture. Since the brightness temperature contrast of the signals of interest can be in the 1-5 K range, sidelobe and spillover losses must be kept to a minimum. A field pattern of  $E(r) = 1 - r^2$  tapered to 0 at the reflector edge will result in sidelobe levels of -25 dB, or 0.9 K, while looking at a 300 K source, and a value of  $k = 1.27$ . Selecting the operating frequency to be 90 GHz and an aperture diameter of 4 m results in a 3 dB beamwidth of 0.001 radian and a ground resolution at 400-km altitude of 423 m.

An offset parabola design was selected to avoid blockage distortions associated with a simple centered parabolic reflector, which would lead to increased sidelobe levels. A large number of feed elements are needed to obtain a wide swath width with many pixels. This requires that the antenna system have

Table 6 -- System Characteristics

	Antenna Size		
	17-meter	10-meter	4-meter
<b>Circular orbit</b>			
Altitude, km	400	400	400
Revisit time, day	144	85	34
Integration time, s	0.007	0.012	0.029
Search rate km <sup>2</sup> /s	65	110	274
$T_{sys}$ rms	0.10	0.08	0.05
<b>Elliptical orbit</b>			
Apogee, km	1000	1000	1000
Perigee, km	400	400	400
Revisit time, day	89	52	21
Integration time, s	0.007	0.012	0.029
Search rate, km <sup>2</sup> /s	104	176	440
$T_{sys}$ rms	0.10	0.08	0.05

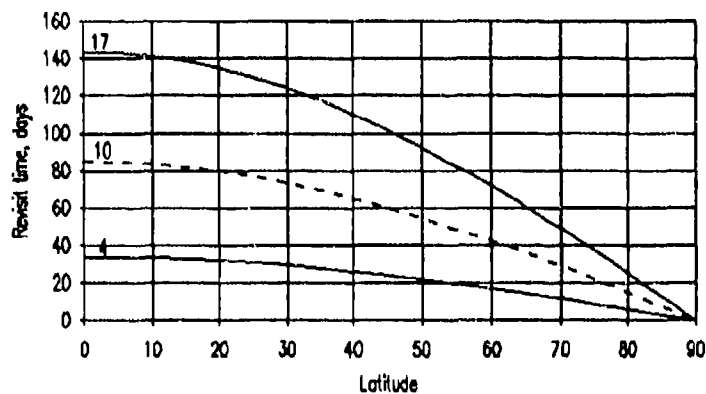


Fig. 1 -- Revisit time

a large  $f/d$  ( $F$  number) to keep the beam aberrations low and to provide good beam-to-beam uniformity. Figure 2 shows the effect of  $F$  number on astigmatism for a two-surface system with  $F$  numbers of 1, 3, and 5. In addition, coma and single-surface astigmatism for an  $F1$  system are also shown for comparison. Astigmatism will be the dominant distortion with larger  $F$  numbers and large off-axis displacements. The aberrations are kept below 1.8 beamwidths for a 50-element-wide array with an  $F$  number of 5. Figure 3 shows a reflector system with an  $F5$  mirror, 4-m in diameter, with a focal length of 20 m. Placing multiple receivers at this distance is unrealistic for a space system and results in large astigmatism. By folding the optics and using an offset Cassegrain design, the receivers and main dish can be positioned together on the main structure and a relatively small, light secondary reflector can be deployed (Fig. 4). The required secondary mirror is 1.4 m in diameter and extends 5.5 m from the main reflector. A major drawback of this design is that the beam spillover from the feeds to the secondary mirror view the hot Earth. By rotating the secondary and moving the receivers to the top of the main reflector, the spillover is directed toward cold space and the system is made more compact. Figures 5, 6, and 7 show the configuration and approximate dimensions for 4-, 10-, and 17-m-diameter reflector systems respectively, which would give resolutions of 423, 169, and 100 m.

The baseline system is designed as a pushbroom imager with 400-m resolution. Characteristics for a 10-m (170-m resolution) and 17-m (100-m resolution) system are included. Other than the reflectors, the three systems would use the same hardware. There are 8 rows of 50 elements with the flight direction in the shorter dimension (Fig. 8). Because the feeds cannot be placed sufficiently close together to get full scene coverage (3 dB crossover), the rows are staggered by one-half a feed spacing and complete coverage is obtained, but with a slight time skew. The multiple rows provide four samples of the scene at different times, allowing various processing schemes such as beam-to-beam differencing and track generation, which require multiple measurements of the scene. Table 7 lists antenna characteristics for the 4-m system.

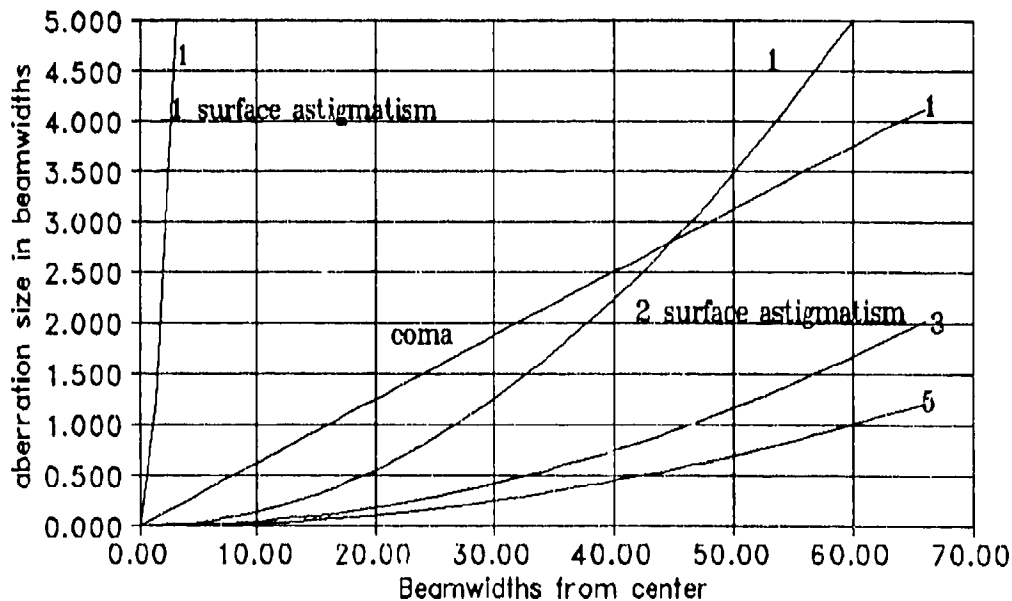


Fig. 2 — Aberrations

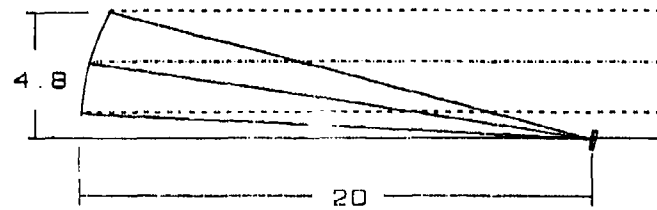


Fig. 3 - F5 parabolic reflector

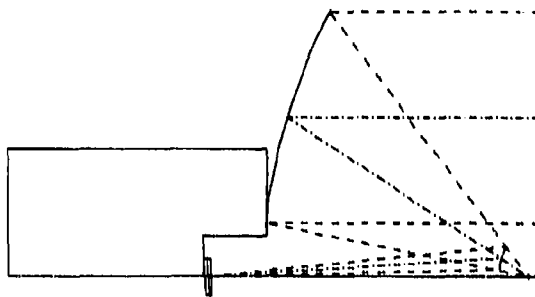


Fig. 4 - Offset Cassegrain

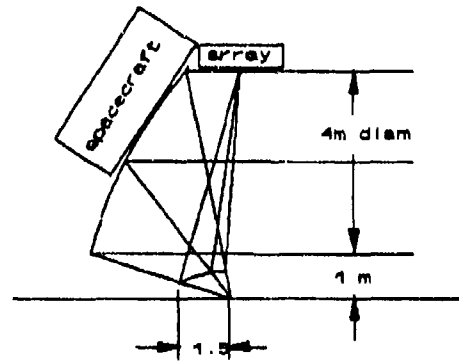


Fig. 5 - 4-m folded Cassegrain

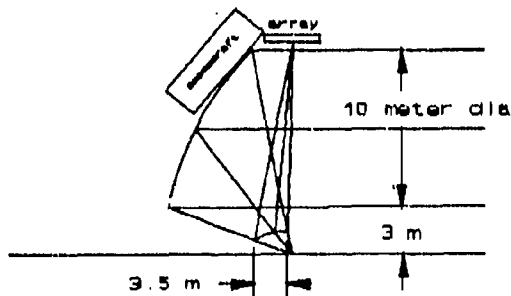


Fig. 6 - 10-m folded Cassegrain

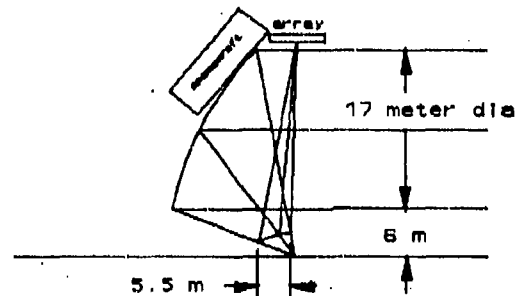


Fig. 7 - 17-m folded Cassegrain

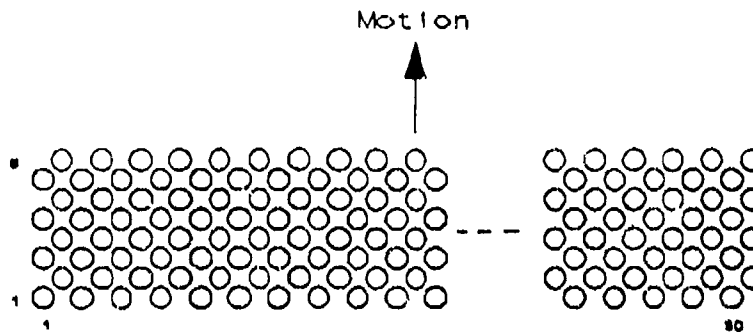


Fig. 8 — System footprint

Table 7 — Antenna Properties—4-m System

Type	Modified offset Cassegrain
Diameter	4 meters
System $F$ number	5
Secondary diameter	1.4 meters
Angular resolution	.001 radian
Resolution @ 400 km	423 meters
Pixel spacing	800 meters center-to-center
Array configuration	50 $\times$ 8 elements
Array size	2.0 m $\times$ .32 m
Swath width	40,000 meters
Corrugated horn	4-cm aperture, 6.2-cm length
Total coma	.0020 radian
Astigmatism	.0006 radian

The receivers are constructed with the mixer integrated into the horn assembly. The intermediate frequency (IF) with a 10 GHz bandwidth is amplified and detected. The receiver has a noise figure of 5 dB, which corresponds to a noise temperature of 630 K. The rms receiver noise for a 30-ms integration time is 0.05 K. Table 8 summarizes receiver specifications. The signal is then amplified by a video amplifier and conditioned by a low-pass filter to the level necessary for the analog to digital converter. The low-pass filter has a cutoff of 18 Hz, which gives a 0.028-s integration time. The signal is then converted to 16 bits at 40 Hz rate and stored for downlinking. With housekeeping data, this gives a downlink data rate of 300,000 bits per second. Table 9 summarizes telemetry, size, and power estimates. Table 10 compares a 4-m system with a 10-m and a 17-m system.

The antenna beams are directed normal to Earth and the integration time is fixed to give Nyquist sampling of the scene at the lowest altitude (highest velocity). The antenna array is composed of 8 rows of 50 beams aligned crosstrack, with alternate rows offset by one-half of the feed spacing to provide Nyquist sampling in the cross-track direction. Figure 9 shows how beam diameter and rms noise level change as altitude increases. Search rate is a trade off with resolution. Figure 10 shows how the search rate for a 50-element-wide array will change as the resolution increases. Figure 11 is a plot of integration time vs reflector diameter for 5 altitudes. Figure 12 shows how rms noise changes as resolution is increased with larger reflectors. Figure 13 plots the resolution and search rate for various sized reflector systems.

Table 8 — Receiver Properties

Frequency	90 GHz
Bandwidth	10 GHz
Noise figure	5 dB
Rms noise level	50 mK
Mixer, preamp	Integral with horn
Size	2.5 × 2.5 × 10 cm

Table 9 — Telemetry, Power, Physical Estimates

Sample rate	40 Hz/pixel
Word size	16 bit
Samples per scan	400
Distance per sample	185 m
Data range	0 - 500 K
Resolution	0.0076 K
TM rate	300,000 bits/second
Power	1500 watts
Weight	200 kg
Deployables	Secondary dish

Table 10 — System Comparisons

	17-meter	10-meter	4-meter
Frequency, GHz	90	90	90
Bandwidth, GHz	10	10	10
Noise figure, dB	5	5	5
Aperture diameter	17	10	4
System <i>F</i> number	5	5	5
Resolution, rad	0.00025	0.0004	0.001
Resolution, m @400 km	100	169	423
Swath width, m	9000	16000	40000
Element spacing, BWs	1.9	1.9	1.9
Array size, elements	50 × 8	59 × 8	50 × 8
Horn size, m	0.04	0.04	0.04
Array size, m	1.8 × 0.61	1.8 × .61	1.8 × 0.61
Secondary diameter, m	5.3	3.5	1.4
Secondary distance, m	23.3	13.7	5.5
Aberrations @ corners	1.8 BW	1.8 BW	1.8 BW
Sample rate, samples/s	290	170	70
Data rate, bits/s	1,500,000	900,000	350,000
Power, W	2000	1500	1500
Weight, kg	350	225	185
Deployables	main dish secondary	main dish secondary	secondary

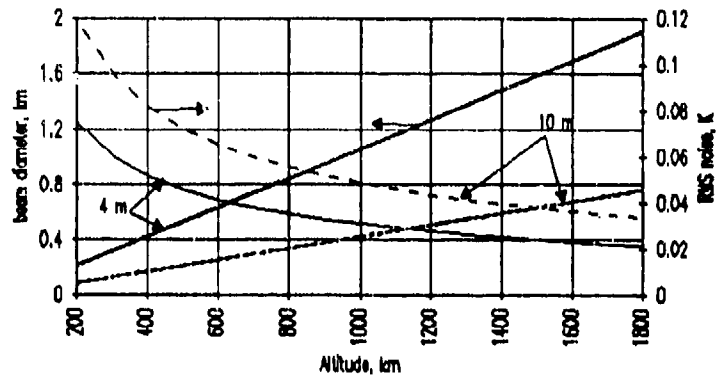


Fig. 9 - Resolution and noise

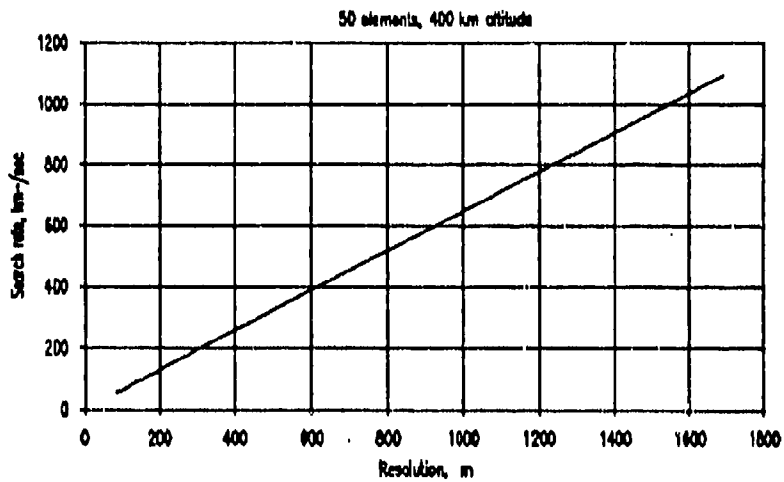


Fig. 10 -- Search rate

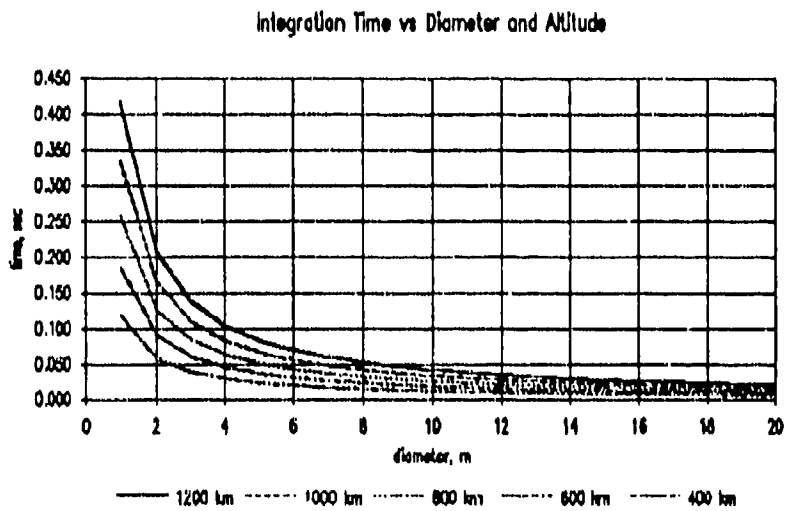


Fig. 11 - Integration time vs altitude

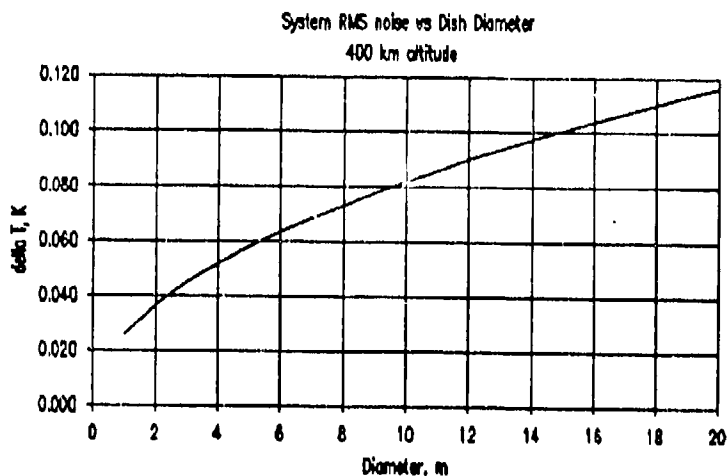


Fig. 12 — RMS noise vs resolution

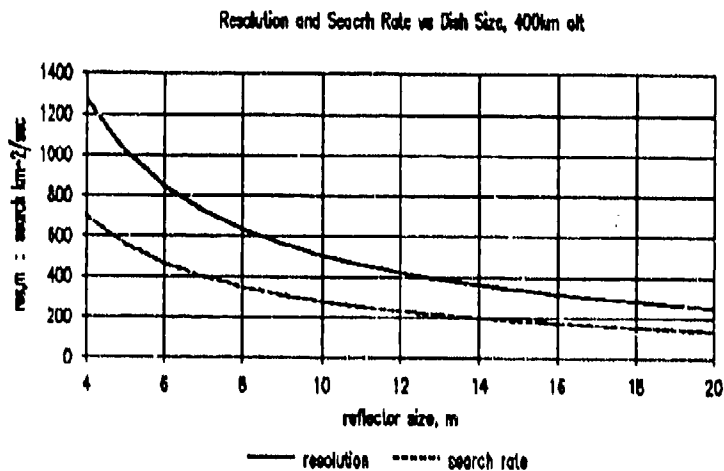


Fig. 13 — Resolution and search rate

## Technology

The reflector system is the only real technological question in producing a high-resolution radiometer system. Present technology can easily produce a 4-m system; with a slight extrapolation, a 10-m system could be built. A 17-m system requiring that both the main dish and the secondary dish be large would be much more complex. A 4-m reflector should be possible without deployment, a reflector larger than 4 m would have to be stowed and deployed in orbit. Work is continuing in the development of large deployable structures; 10-m appears to be near future, 17-m could be several years off. It should not be a problem to deploy the secondary reflector for the 4- or 10-m system with a 1.4- or 3.5-m subreflector. The 17-m system will be a much more complex system, with two large reflectors and a secondary reflector mounted up to 23 m from the space craft. This must tolerate dynamic alignment problems from thermal and mechanical stresses. The feeds are standard horns of reasonable size. The mixer-preamps are fairly common, however units with 5 dB noise levels are state of the art at present but should become

common in the near future. A 10 GHz IF is not a problem, and video amplification, detection, and digitization is standard. Data rate is well within the current capabilities. Pointing information of the order of .0001 radian must be obtained if overlaying of data is required.

MMIC will soon be practical at W band and could be used to eliminate the mixer, thus lowering noise levels and power requirements while decreasing size and weight. This technology is still several years away for practical use.

### Tradeoffs

Table 11 shows how some of the system features change as the resolution increases. The magnitude column gives an idea of how fast the feature changes as the resolution is increased by a factor of  $N$ . The impact column is a qualitative estimate on how this change effects the system viability, i.e., is it a show stopper. Changes in integration time, system noise, and transmission (TM) rate are all related and do not drive any technical limits. The TM rate increase can easily be handled, while background clutter noise will be large compared to the increased system noise. Weight and system complexity will go up, but they should be manageable. Swath width can be partially compensated for by adding beams, but this has a limit and may increase system size or decrease performance. Search rate and revisit times are major losses with increased resolution, and program needs will dictate if the system is operationally sound. Active pointing could be used in some applications to increase revisit times for limited areas. Cost may be prohibitive for the higher resolution systems. The large apertures will require large deployable structures and a great deal of development work. System pointing requirements will also become more severe as the resolution is increased.

Table 11 — Takeoffs for Increased Resolution -  $N$

Feature	Effect	Magnitude	Impact
Integration time	▼	$1/N$	-1
System noise	▲	$N^{.5}$	0
Tm rate	▲	$N$	0
Swath width	▼	$1/N$	-3
Search rate	▼	$1/N$	-3
Revisit time	▲	$1/N$	-3
Signal/noise	▲	$N^{1.5}$	2
Weight	▲	$N/2$	-1
Complexity	▲	$N^{1.5}$	-2
Cost	▲	$N^{2.5}$	-5

## TARGET AND BACKGROUND CHARACTERISTICS

### Millimeter-wave Images

Figures 14 through 16 provide examples of scene brightness temperature contrast at 90 GHz. All three were obtained from an aircraft by using a single scanned beam. The surface resolution is about 15 m and, with one exception, the false color code for all of the images begins with blue (coldest) progressing through green, yellow, and orange, to red (warmest). The one exception is Fig. 15 where the coldest temperatures, such as oil tanks and the docked ships, are colored pink. In general, metal surfaces appear coldest at millimeter wavelengths; water is at intermediate temperatures and turbulent

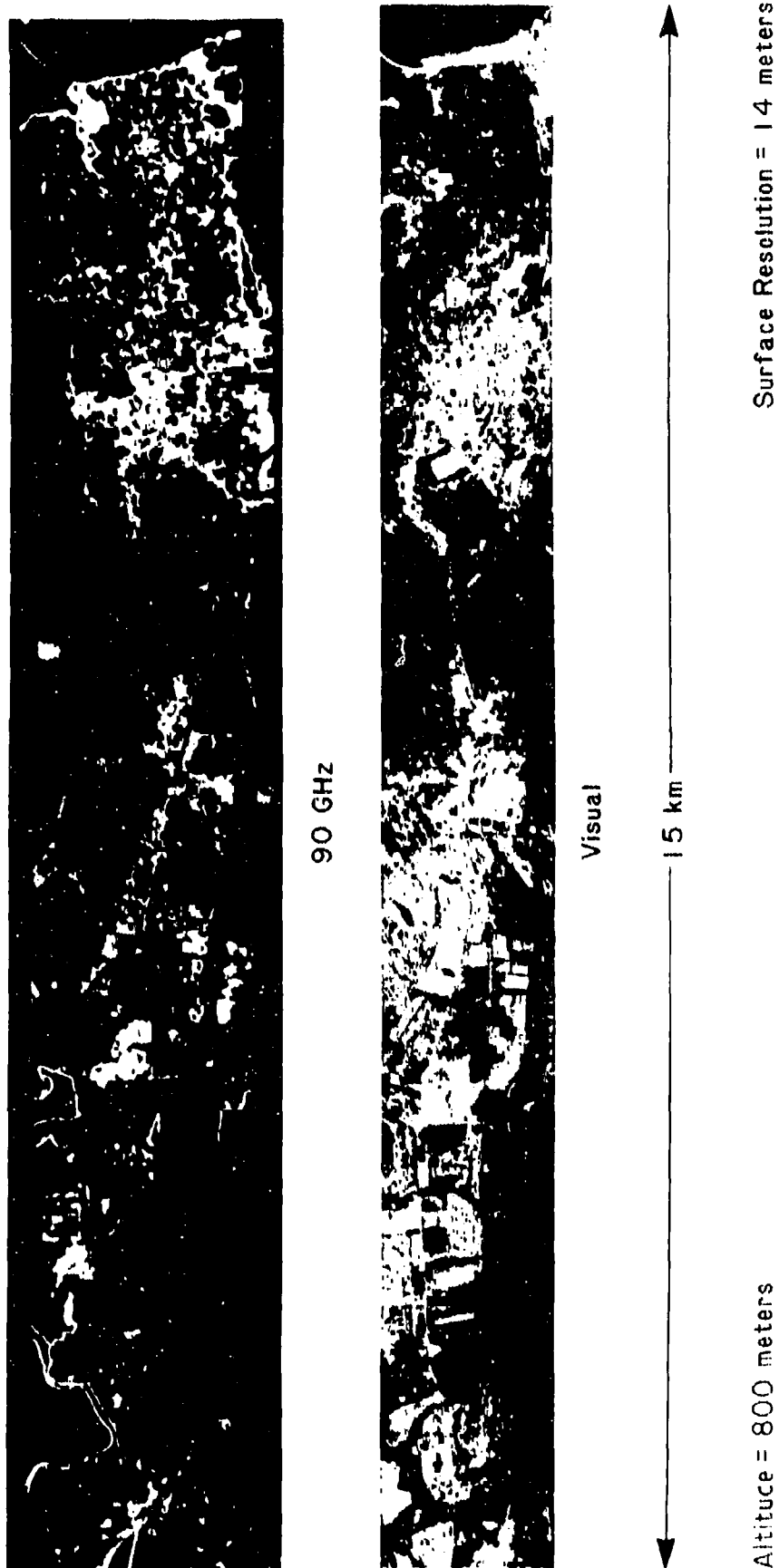
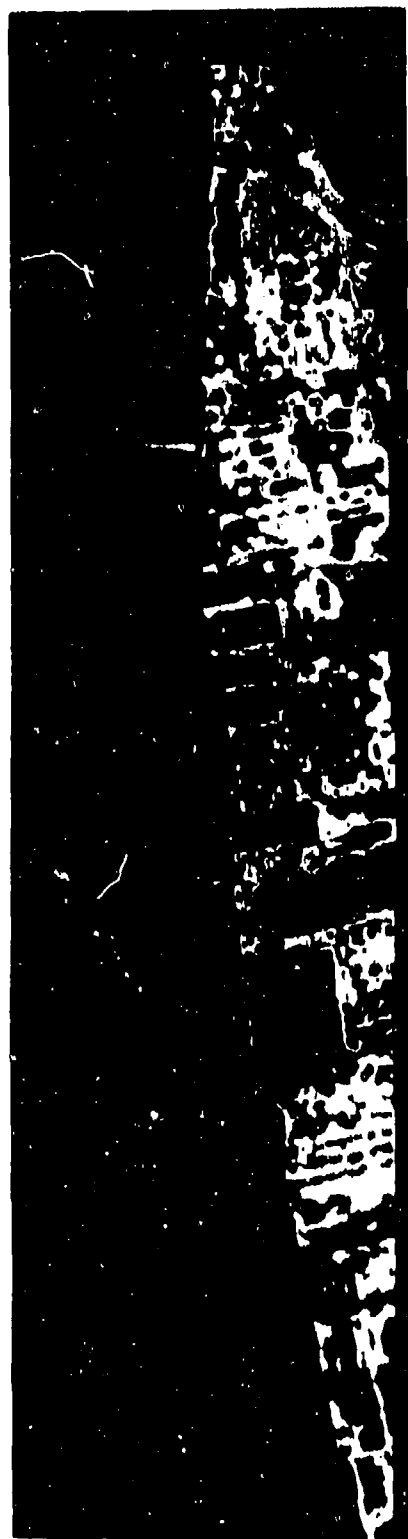


Fig. 14 — 90 GHz imagery of Portsmouth, Virginia



90 GHz



Visual

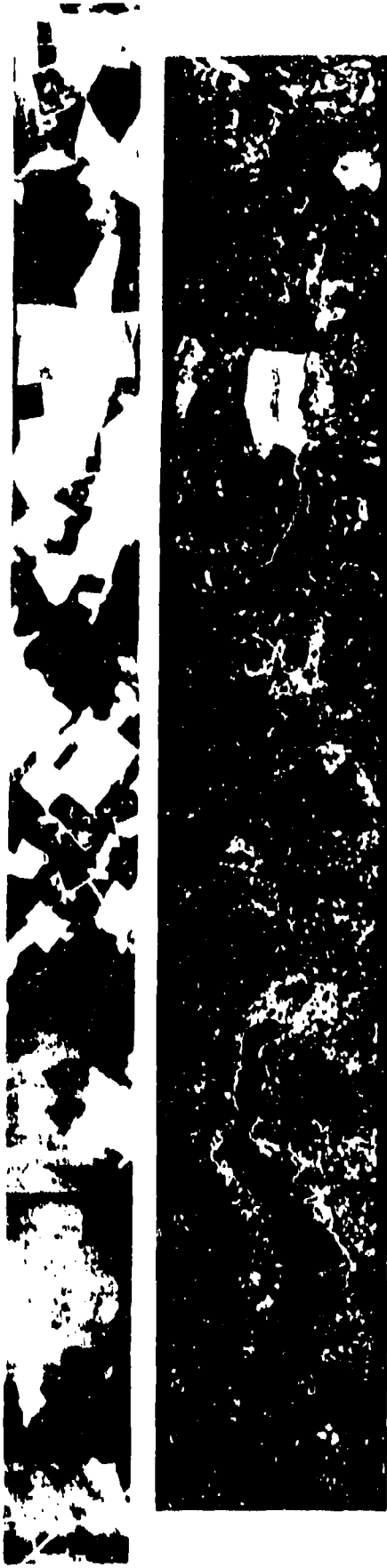
6.7 km

Altitude = 800 meters

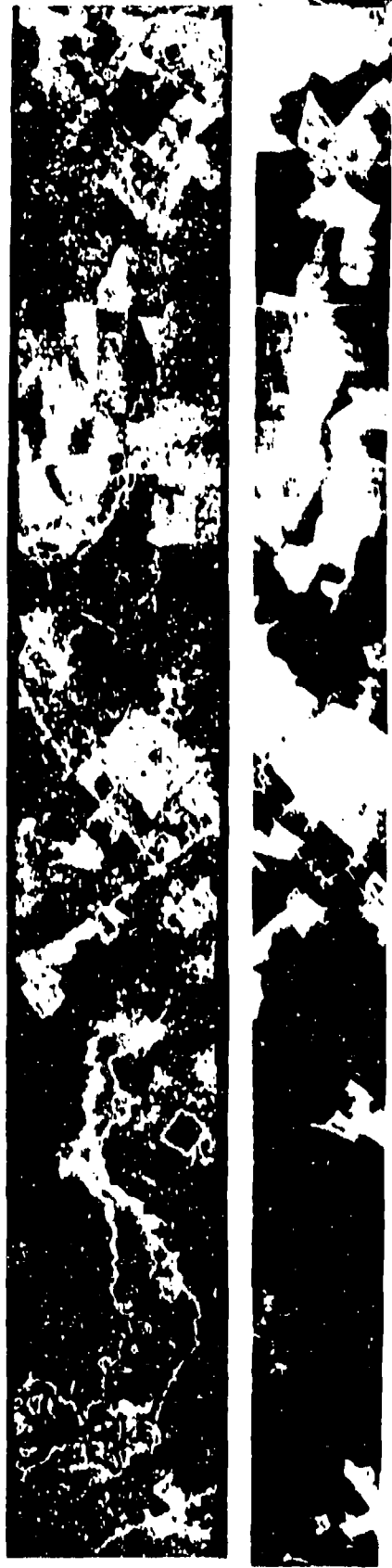
Surface Resolution = 4 meters

Fig. 15 — 90 GHz imagery of the docks at Norfolk, Virginia

90 GHz IMAGERY AND CORRESPONDING PHOTOGRAPHS  
IDENTICAL REGION FOR BOTH SPRING AND WINTER



APRIL 1980



JANUARY 1981

13 km

Altitude = 870 meters

Surface Resolution = 12 meters

Fig. 16 — 90 GHz imagery of Virginia farmland in January and April

white water and terrain are warmest. Note that this is the apparent millimeter-wavelength radiative temperature, not the physical temperature of the material. Accompanying each image is coincident photography. The image in Fig. 14 of Portsmouth, Virginia, shows highways, buildings, and open areas in the city. The brightness temperatures  $T_B$  range from 186 to 288 K. Notice the cloverleaf intersection to the left of center in the image. The dots on the road leading out of the interchange are trucks. The image in Fig. 15 of the docks at Norfolk shows docked ships, oil storage tanks, buildings, parked cars, and grassy areas on the docks. Here the  $T_B$  range is 168 to 279 K. The two aircraft carriers at the extreme right are distinguishable in the imagery by their shape. Also note that the island superstructure of the aircraft carriers is recognizable. The images in Fig. 16 of Virginia farmland show identical areas for both spring (April 1980,  $T_B = 180$ -295 K) and winter (January 1981,  $T_B = 189$ -277 K). For this set of images, purple represents brightness temperatures intermediate between those represented by blue and green. Ice on the lake at the left of the winter image shows as purple, while in spring, swampy areas there show as purple. Furthermore, emissions from the farm fields are similar to the surrounding forest in the spring (both are reds and yellows). However, during the winter, the open farm fields appear colder (green) than the surrounding areas (red). In general, the 90 GHz images closely resemble the detail and form of the visual image. This makes the millimeter-wave imagery particularly easy to interpret and greatly facilitates use of imagery by relatively untrained observers.

## Clutter

### *Surface Clutter*

Variations in the reflectivity, emissivity, scattering, and absorption of the surface and atmosphere constitute a clutter background against which the target must be identified. The wide range of size, shape and contrast of land features is clearly visible in Figs. 14 through 16. Examples of background clutter spectra are given in Figs. 17 through 19 for farmland, sea ice, and docks. Note the similarity of the shape of the spectra and that the power is greatest at the lower spatial frequencies. A target with dimensions of 100 m or smaller has spectral power primarily at spatial frequencies of 10 Hz/km or higher where the background clutter is relatively small. This provides a means to suppress the clutter by matching the spatial frequency response of the receiving system to that of the target and rejecting the lower spatial frequencies of the background clutter. The ocean presents a more uniform background than land, but clutter is generated primarily by breaking waves and atmospheric variations such as clouds, rain cells, and water vapor density variations. In order to detect targets near or at the limits set by the receiver sensitivity, the background clutter must be suppressed. To do this, the characteristics of the receiver must be matched to some property that is unique to the target and is not present or is present to a lesser degree in the background. This property may be the size and shape of the target, the amplitude, polarization, or frequency spectrum of its radiation or the time variation of any of these. If the target is moving relative to the background, the clutter may be suppressed by using an array of beams. This technique relies on repeated differencing of the signals from successive beams as they sweep over the scene. Those features, which change very slowly compared to the time delay between beams, such as spatial clutter, will be subtracted out whereas a target which has moved relative to the background in the time between successive measurements will present a signal. By using this technique, clutter rejection of as much as 23 db has been obtained at 10 GHz with an aircraft real multiple-beam system here at the Naval Research Laboratory. Figure 20 shows an example of these results. The unshifted output from two of the beams, one of which trails the other by two beamwidths, is shown at the top of the figure. The result of subtracting the signal from the first beam, appropriately delayed, from the signal from the trailing beam is shown in the middle of the figure. The clutter has been reduced by more than an order of magnitude, and the target signal is apparent. The horizontal S-shaped response to the target is due to differencing the signal from the two beams. The large spurious deflections are due to aircraft pitch, roll, and yaw motions

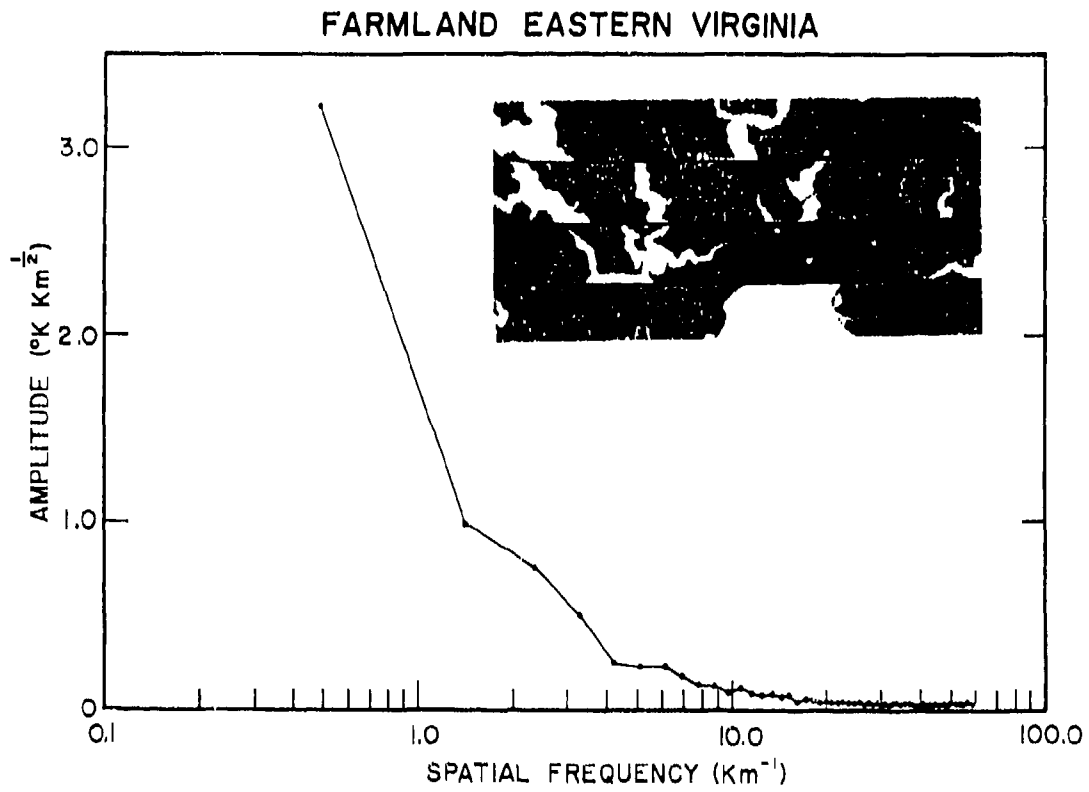


Fig. 17 — Spatial clutter spectrum of farmland at 90 GHz

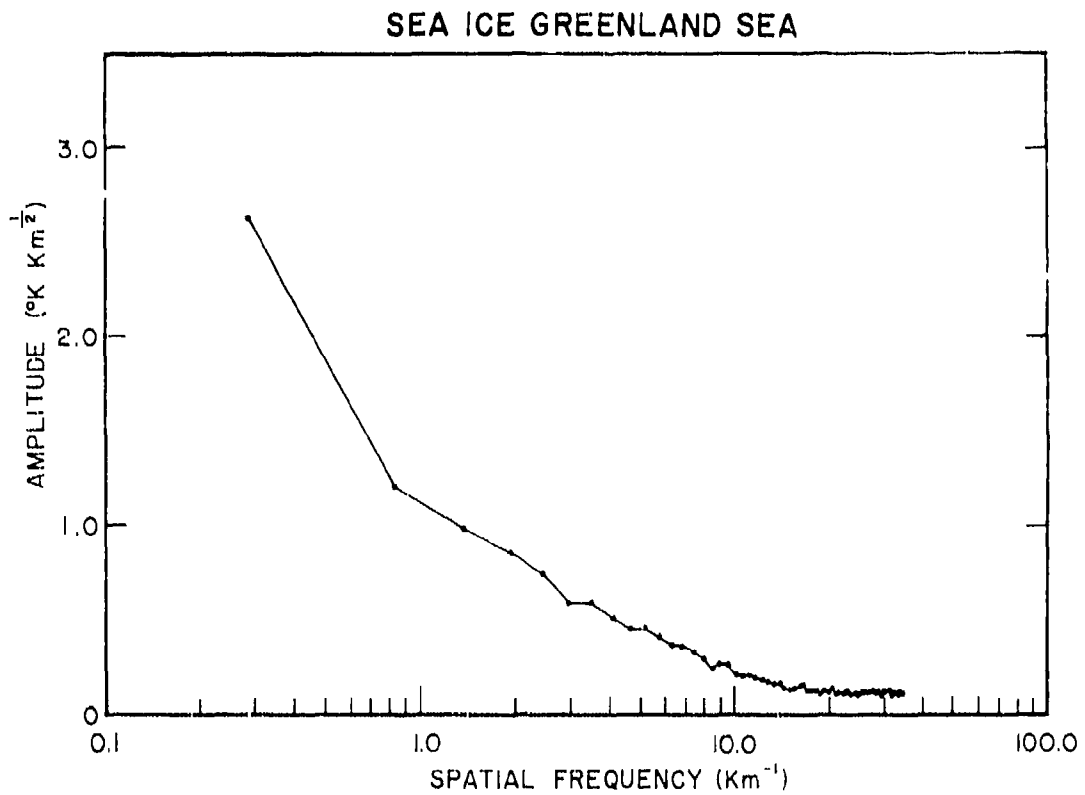


Fig. 18 — Spatial clutter spectrum of sea ice at 90 GHz

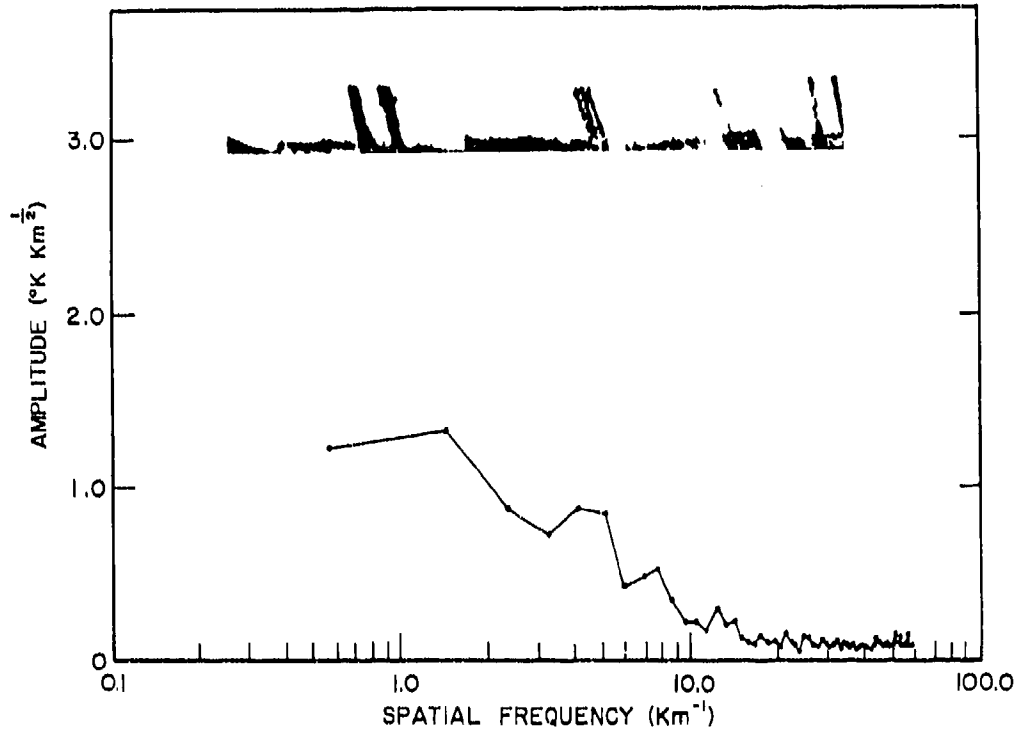


Fig. 19 — Spatial clutter spectrum of dock area at 90 GHz

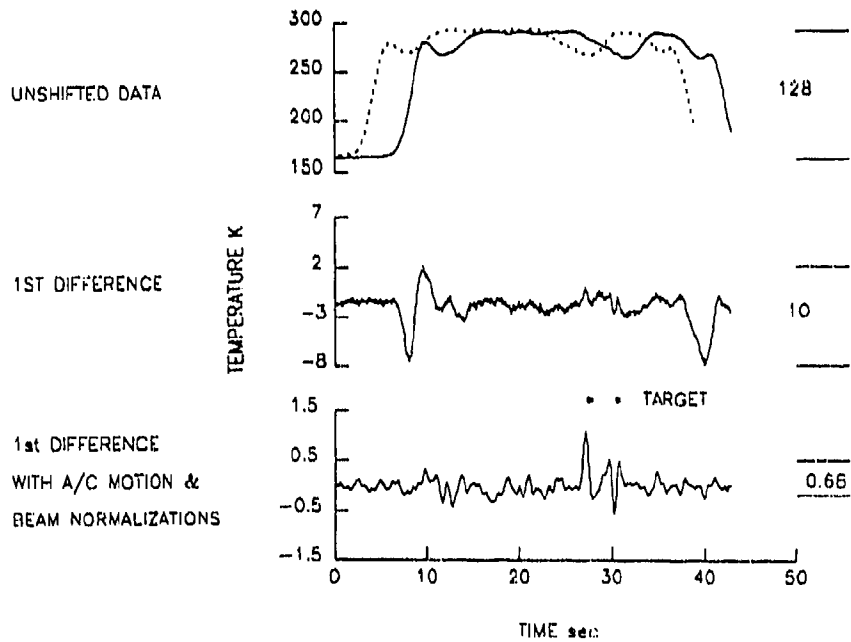


Fig. 20 — Clutter suppression using beam differencing

and to slight differences in the shape of the two antenna beams. The signal after correcting for these effects is shown at the bottom of the figure. The target signal is now clearly visible, and the remaining noise is almost entirely due to instrument noise.

### *Atmospheric Temporal Variations*

Atmospheric variations in temperature, pressure, and humidity cause fluctuations in the millimeter-wave radiation received from the atmosphere and from background scenes. These fluctuations in the emission and absorption of the atmosphere place limits on the ability of passive millimeter-wave radiometers to detect targets in a noisy environment that are in addition to the limits imposed by instrumental noise and surface clutter described above. Upward-viewing measurements of the sky at 37 GHz for three groups of atmospheric conditions ranging from clear, group 1, to intermediate light clouds, group 2, to heavy clouds, group 3, are shown in Fig. 21. Note that the power spectrum shown at the top of the figure, while relatively flat for clear sky, shows increasing energy at low frequencies up to about 0.1 Hz (10-s period) with increasing atmospheric congestion. The temporal structure function  $D(\tau)$  is a way to characterize a nonstationary random process, such as atmospheric turbulence, by taking the rms difference between the time-dependent function and itself at a later time. It is given by  $D(\tau) = \{f(t+\tau) - f(t)\}^2$  where  $\tau$  is the time lag. The temporal structure function analysis  $R(\tau)$  is a means of removing the instrumental noise to obtain the true contribution of the sky. It is given by  $R(\tau) = \text{sqrt} \{(D_s(\tau) - D_i(\tau)) / D_i(\tau)\}$  where  $D_s$  and  $D_i$  are the temporal structure functions of the scene and instrument. When  $R$  is greater than unity, the temporal clutter of the sky exceeds that of the instrument. In particular, the value of 7 for which  $R = 1$  represents the approximate maximum useful integration or sample time for the scene. As can be seen in the lower half of Fig. 21, this may be as short as a few seconds for heavy clouds. This is shown further in Fig. 22 where the rms of the measured signal is given as a function of integration time. Note that, for heavy atmospheric clutter, the rms signal actually increases for integration times greater than about a second or so. In conclusion, sky temporal clutter may dominate system noise for integration times greater than a few seconds. Longer integration times are not effective in decreasing system noise and increasing signal-to-noise ratio since increasing the integration time will not necessarily reduce sky clutter noise. Therefore, there is a limit to the reduction of the minimum detectable signal obtained by increasing the integration time. Further increases of sensitivity will have to be achieved by other means. The nonstationary nature of temporal variations of atmospheric emission does not preclude the possibility of clutter suppression. However, a detailed knowledge of the spatial and temporal clutter of the atmosphere and of background scenes is needed so that matched filtering in both the spatial and temporal domains can be used to enhance the signal-to-clutter ratio.

### **Military Targets**

#### *Aircraft, Tanks, and Vehicles*

These targets are generally made of metal. Metal, even when painted, appears as a mirror to millimeter-wavelength radiation; it reflects radiation while radiating little because of its own temperature. The signal will depend on the orientation of the surface and what is in the reflected field of view. In most cases, for space surveillance systems, the surface is viewed parallel or nearly parallel with Earth's surface. Therefore, it will reflect only the radiation from the atmosphere and space, making metal surfaces appear to be much colder than the surrounding surface. An exception is when an absorbent coating is used on the metal, giving it a high emissivity where the signal will represent the temperature of the target rather than the reflected scene. Table 12 lists characteristics of some selected military targets. The following discussion of military target detectability assumes that environmental clutter has been suppressed and that only instrumental noise is present.

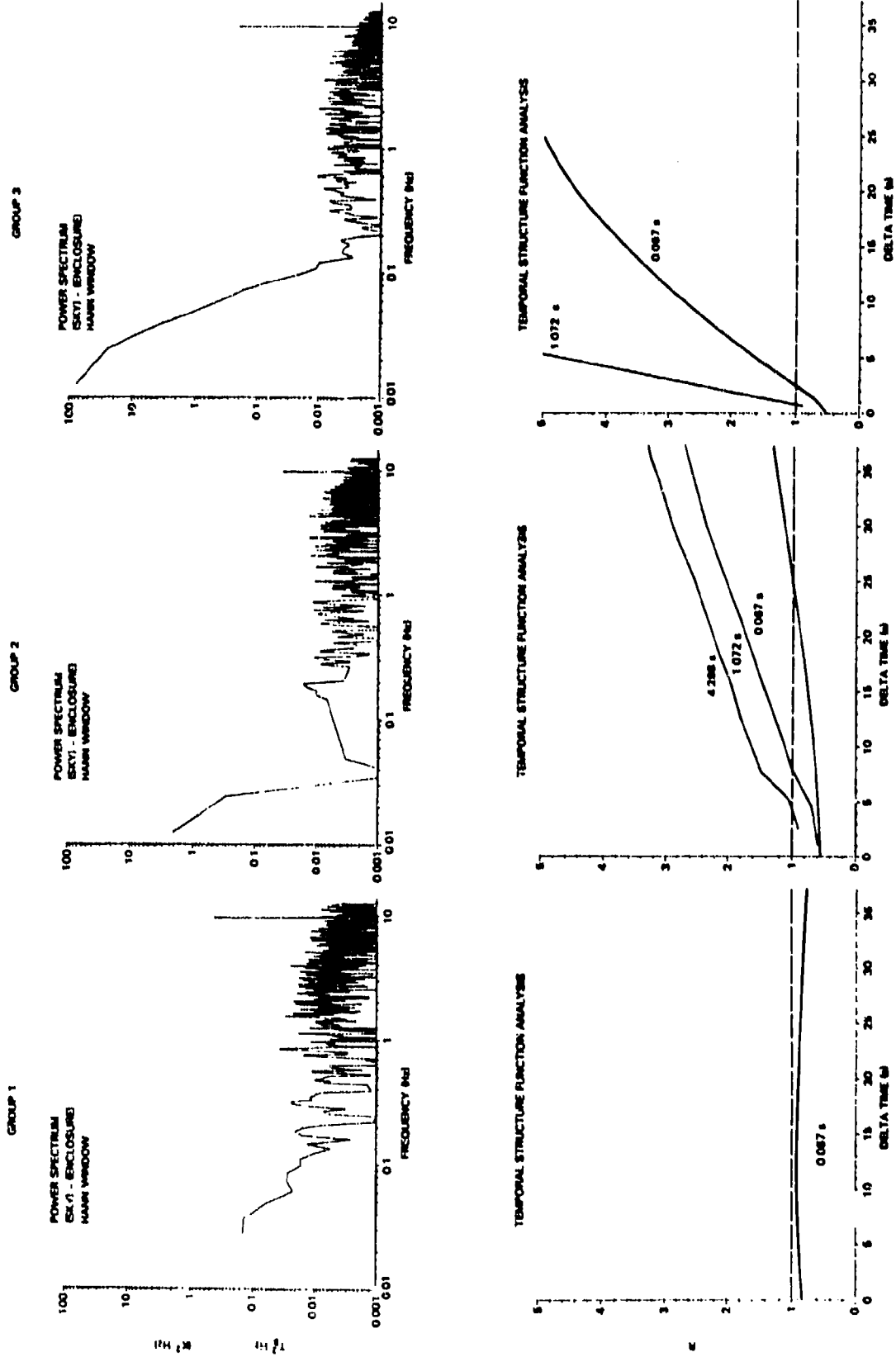


Fig. 21 - Atmospheric clutter analysis for three sets of atmospheric conditions

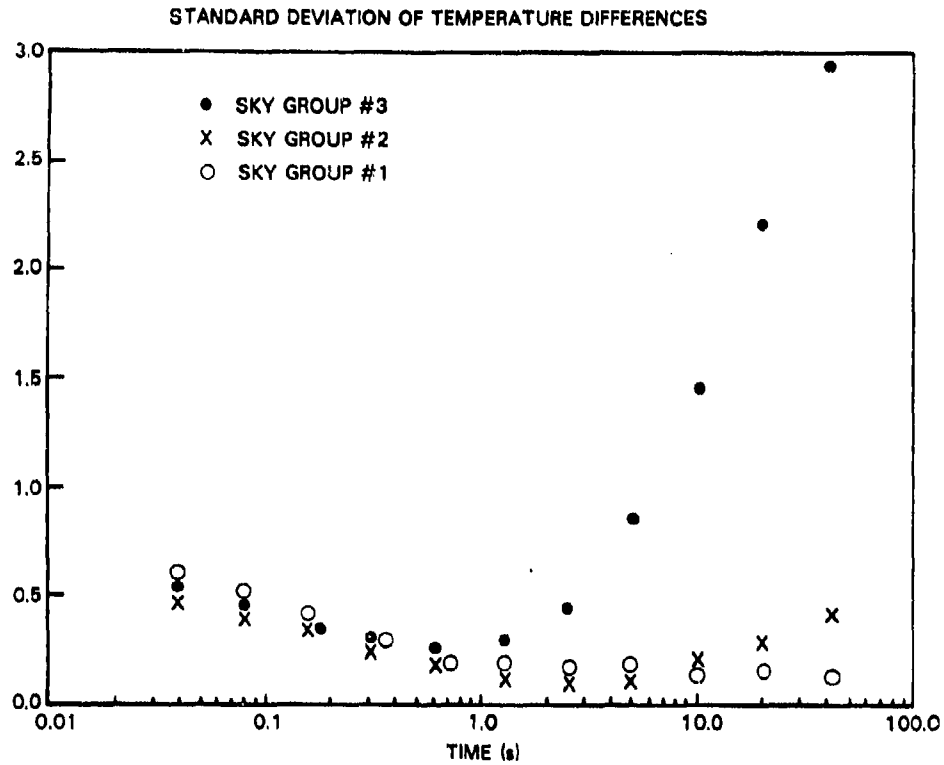


Fig. 22 — Atmospheric clutter noise increase with increased integration time

Table 12 — Characteristics of Military Targets at 90 GHz

Target	Area (m <sup>2</sup> )	Emissivity	Temperature (K)
Aircraft carrier	8400 - 13700	0	290
Battleship	9000	0	290
Missile cruiser	3400	0	290
Destroyer	1300	0	290
Attack boat	260	0	290
FT boat	185	0	290
Patrol boat	30	0	290
Ship wake	Up to 3000+	0.9	290
Ship atmos. wake	Beam fill	0.7 - 0.9	283
B-52	800	0	290
Backfire bomber	400	0	290
F-117A fighter	108	0	290
F-15E fighter	83	0	290
Tank	15	0	290
Car	12	0	290
Missile	10	0	290
Mines	1	0	290
Troop concentration	100/company	1.0	290
Buildings	2500	0.87	290
Airport/runways	50000	0.9	290
Fires/battlefield	10000	> 0.9	700
damage assessment			

Figures 23 through 28 show the high contrast signal of vehicles and aircraft obtainable with high spatial resolutions. Figure 23 shows individual aircraft and vehicles at 34 GHz with a resolution of about 10 m. Measurements of a P-3 aircraft at 90 GHz over both land and water backgrounds are given in Fig. 24. The resolution is 3 m in all flight strips in Fig. 23 except the fifth and sixth strips where it is 10 m. The signal contrast of the same P3 at 140 GHz and 3 m resolution is shown in Fig. 25. Figure 26 is an image of an aircraft on a pedestal, viewed from slightly below at 90 GHz with 0.5-m resolution. The bottom of the aircraft appears much warmer than the top; it is reflecting the relatively hot radiation from Earth's surface rather than the cold sky as does the upper surface. Images of automobiles at 90 GHz and 0.5-m resolution are given in Figs. 27 and 28. The vertical feature between the two autos in Fig. 27 is the signal from a man. The beam-fill contrast temperatures for the aircraft and vehicles in these figures is very large—as much as 80 K over water and 120 K over land. The atmospheric loss is  $\alpha = 1/3$  for this imagery, although it typically ranges from 1/3 to 2/3 under cloudy conditions depending on season and latitude, as given in Table 1.

To estimate the signal-to-noise ratio (S/N) [as given by Eq. (14)] for various military targets, a typical value of  $\alpha = 1/2$  is used. This results in an atmospheric factor of  $(1 - \alpha)^2 = 0.25$ . The difference in temperature between the target and background,  $\delta T$ , is taken as 0 and the temperature of the background as 290 K. The emissivity of the oceanic background varies from about 0.55 to 0.68 for calm conditions, depending on temperature. It is 0.6 at 290 K. Under high sea states, emissivity increases to 0.8 or more. The emissivity of the land background ranges from about 0.55 to 0.93 (Table 2). An average value of 0.75 is used for the emissivity of the background. Table 1 gives the emissivity of the target. The denominator of Eq. (14) is the instrumental sample noise. It is given as 0.10 and 0.05 K for the 100- and 400-m resolution systems, respectively, in Table 6. These values result in a S/N, for a metal target with 0 emissivity, of 0.027 and 0.0034 times the area of the target in  $m^2$  for the 100- and 400-m resolution systems, respectively. The 400-m baseline system with a 4-m antenna is 8 times less sensitive than the 100-m resolution system using a 17-m antenna.

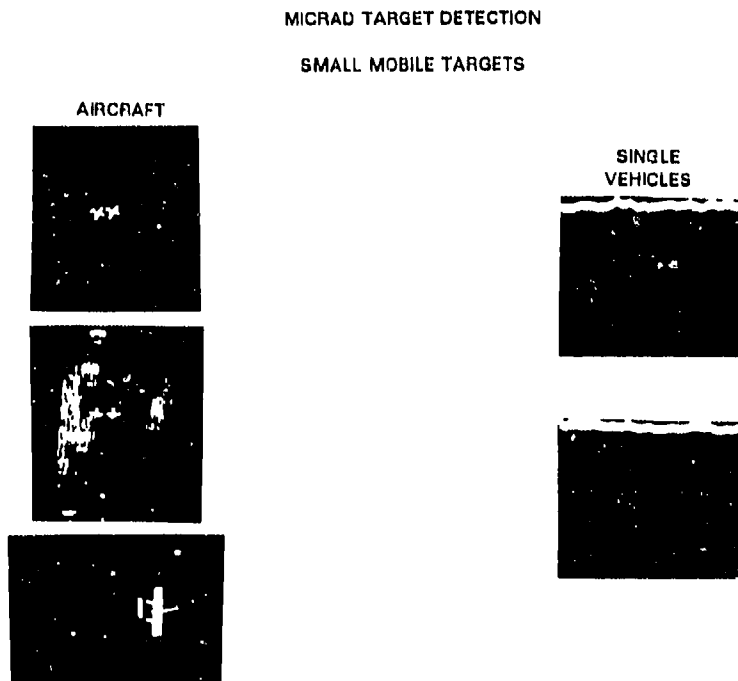


Fig. 23 — 34 GHz imagery of aircraft and vehicles

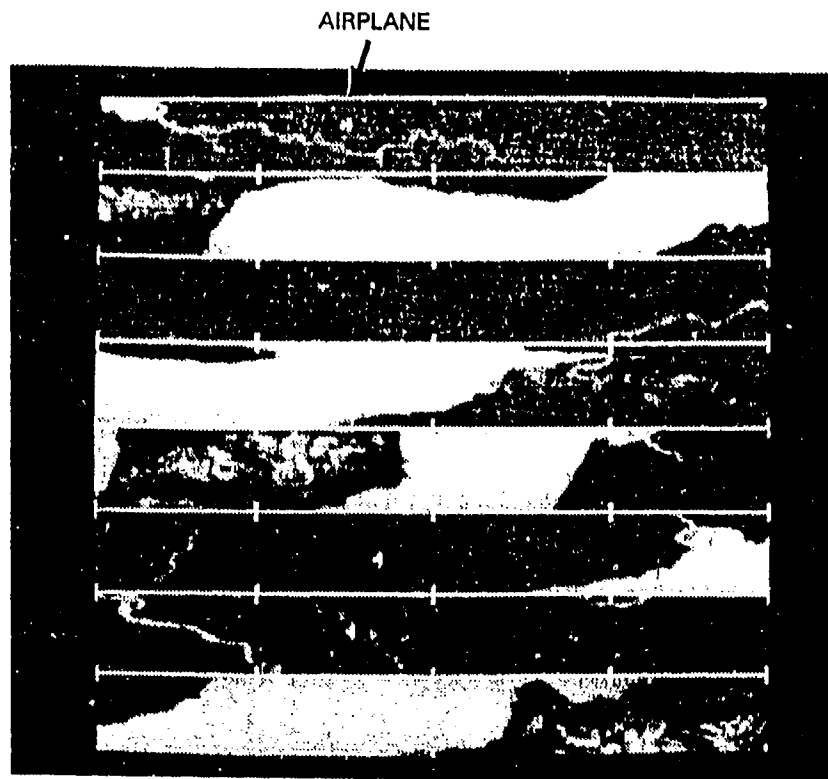


Fig. 24 -- 90 GHz imagery of an NRL P3-A aircraft over land and sea backgrounds

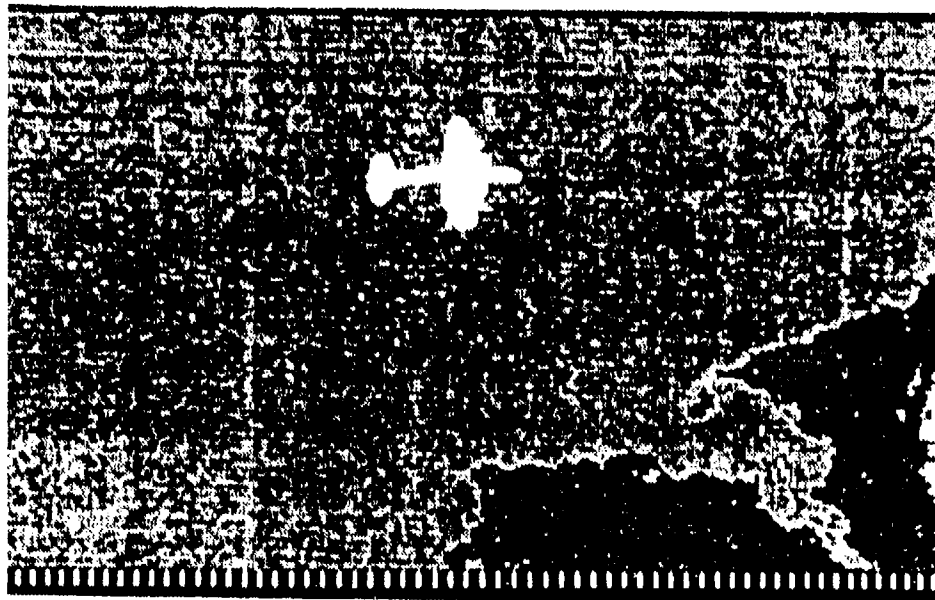


Fig. 25 -- 140 GHz imagery of an NRL P3-A aircraft over water

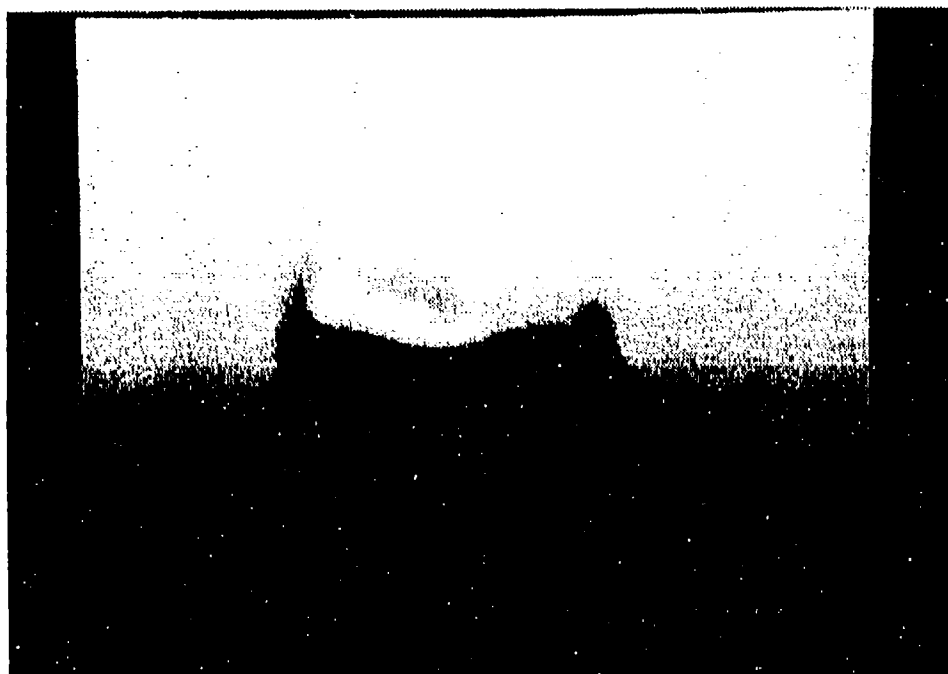
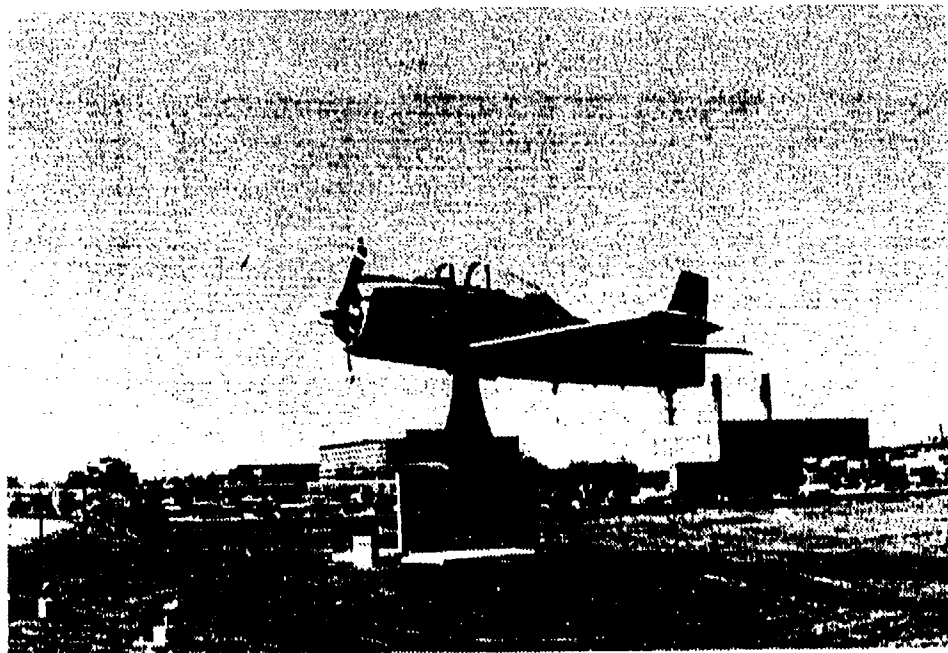


Fig. 26 — Very-high-resolution 90 GHz imagery of a pedestal-mounted aircraft



Fig. 27 — Very-high-resolution 90 GHz imagery of automobiles and man

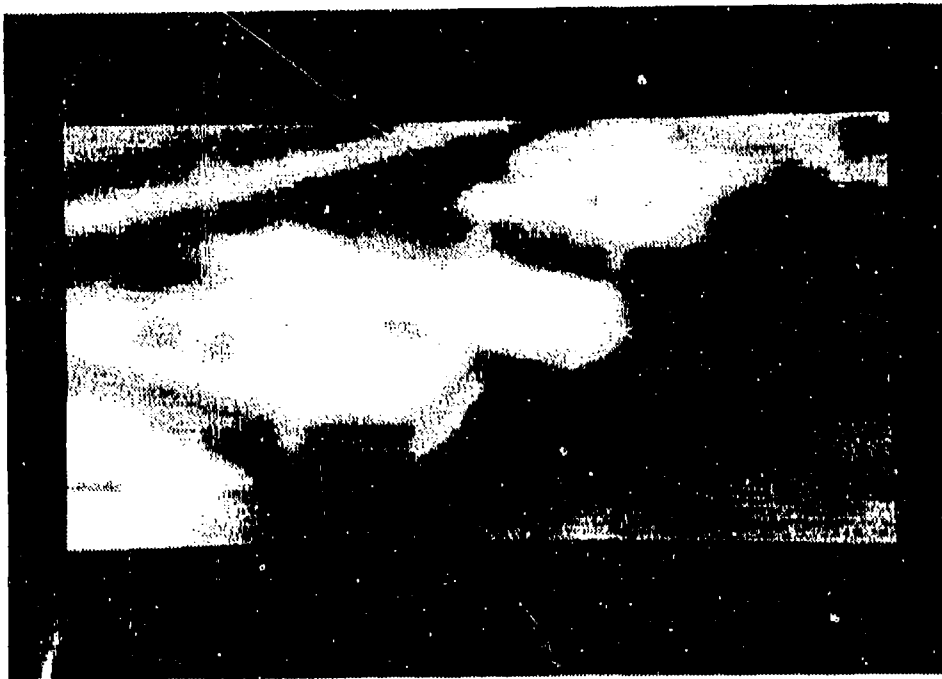
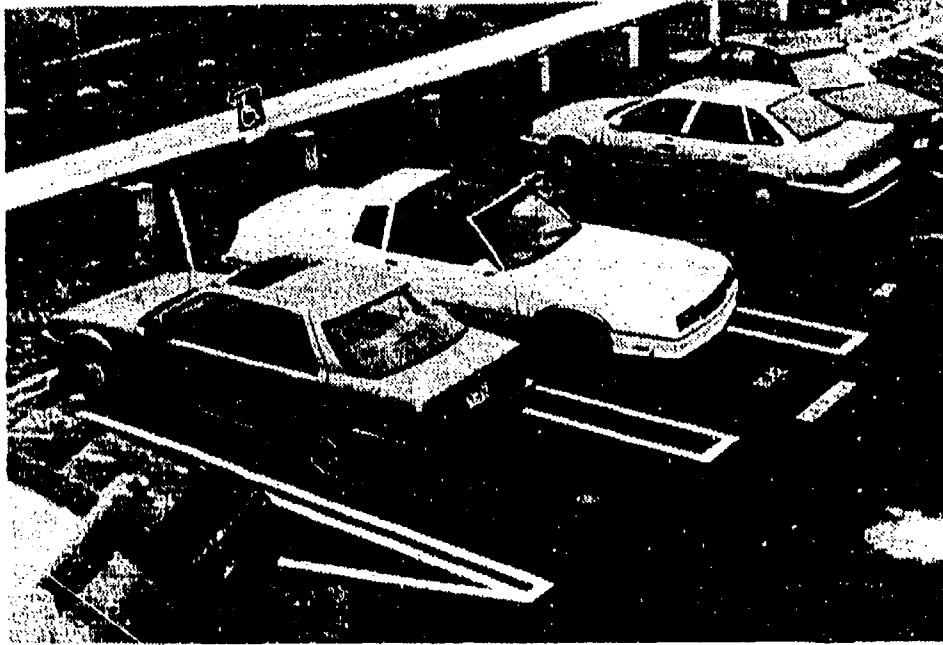


Fig. 28 — Very-high-resolution imagery of a parking lot

Under these conditions and with clutter suppressed, aircraft are detectable with the 100-m resolution baseline system. For example, the area of a Backfire bomber (a large aircraft) is about  $400 \text{ m}^2$ , resulting in a  $S/N = 11$  for these unresolved targets. To put this in perspective, a  $S/N$  of 6 is required to obtain a probability of threshold detection, 0.5, with a false alarm rate of  $10^{-9}$ . However, for the baseline system with a resolution of 400 m, the  $S/N$  is only a little more than 1. Thus a single Backfire bomber is practically undetectable. However flights of about five or more would be detectable if they were within the 400-m resolution cell. Single fighters with an area of only about  $100 \text{ m}^2$  would not be detectable with either system, nor would tanks and vehicles with an area of  $\sim 15 \text{ m}^2$ . An area of about  $220 \text{ m}^2$  or greater is required to obtain a  $S/N$  of 6 at 100-m resolution. The 400-m resolution system requires a target with an area greater than  $1800 \text{ m}^2$ ; thus single tanks or vehicles are not detectable. Massed groups of 20 or more would be detectable if concentrated within the 100-m resolution cell. Eight times as many would be required for detection with the 400-m resolution system.

### Ships and Ship Wakes

Metal ships appear as a cold contrast against the sea. The foam from the ship wake or breaking waves has an emissivity greater than the undisturbed sea and will appear to be warmer than the surrounding sea. Figure 29 shows images of the aircraft carrier *Constellation* through clouds at 34 GHz and with a resolution of 10 m. (Aircraft carriers as well as other ships are seen at the docks in Fig. 15.) The area of an aircraft carrier is in excess of  $8400 \text{ m}^2$ . Therefore, the contrast temperature is more than twenty times larger than a Backfire bomber and is easily detectable, even with the 400-m resolution system. In fact, the 100-m resolution system can resolve an aircraft carrier and provide contrast temperatures of tens of degrees. Ships as small as an attack boat, with an area of  $260 \text{ m}^2$  are detectable at 100-m resolution, while something approaching the size of a missile cruiser is required for detection at 400-m resolution.

Figure 30 shows an image of a ship and its wake at 90 GHz. The brightness temperature of the turbulent wake here is as much as 60 K above the sea background of 199 K, and temperatures in excess of 10 to 20 K can be expected in general. This wake is 15 km long implying a persistence of one-half hour or more. Contrast temperatures of turbulent wakes longer than about 200 m will be several degrees for the 100-m resolution baseline system; those longer than about 800 m will be nearly a degree for the 400-m system. Thus,  $S/N$  ratios of 10 to 20 will result. Ship wakes with lengths of kilometers will be many samples in extent; this will enhance recognition and effective  $S/N$  ratio greatly and make them readily detectable.

The signal from the Kelvin wake of a ship is much weaker than the turbulent wake. Figure 31 shows the 90 GHz signal from a modeled Kelvin wake of a destroyer at 15 knots under both calm sea and 12-knot winds. The calm sea case is also shown in profile in Fig. 32. The model is based on a representation of the wake and sea surfaces as a collection of plane facets with dimensions of  $5 \times 5 \text{ ft}$ . Although a few individual facets may have brightness temperature contrasts in excess of 20 K, the integrated contrast over the entire wake is only 0.6 and 0.4 K for the calm and rough ocean, respectively. This indicates that, despite the crudeness of the model, the Kelvin wake may be detectable with the baseline system. It should be noted that although the turbulent and Kelvin wakes present positive contrasts above the background, the ship contrast will generally be negative. Therefore, the net signal in a resolution cell may be reduced and may possibly even be zero.

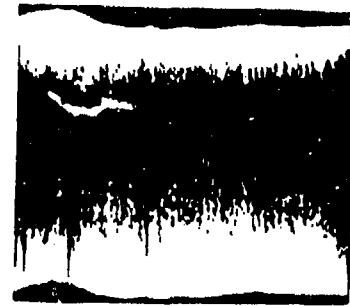
## CARRIER CONSTELLATION THRU CLOUDS



MICRAD



AERIAL PHOTO



MICRAD

Fig. 29 — 34 GHz imagery of the aircraft carrier *Constellation*

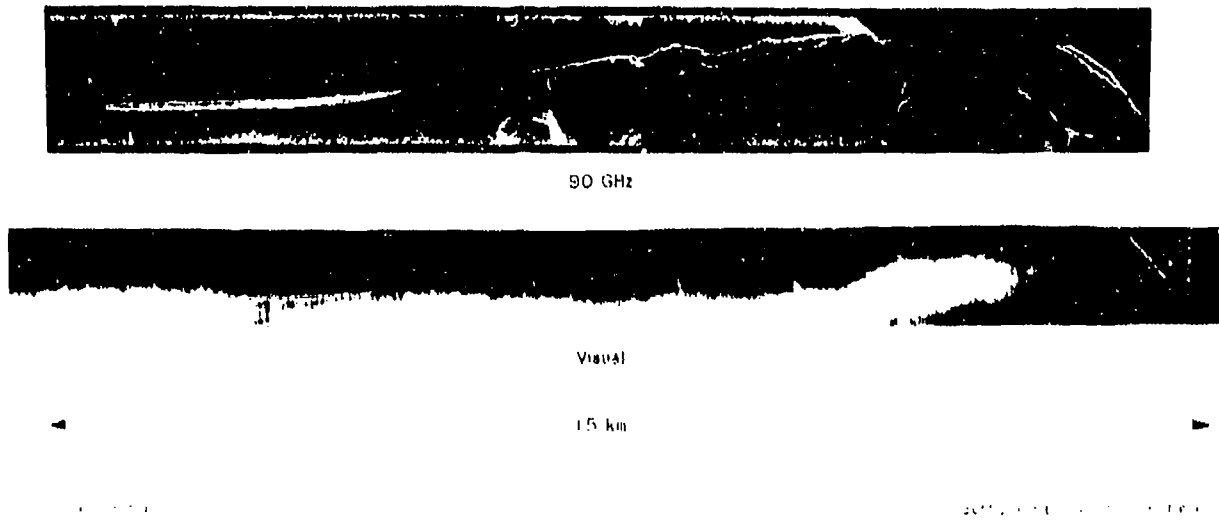
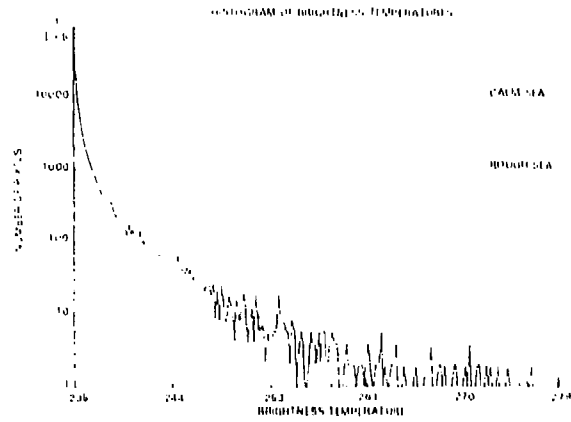


Fig. 30 -- 90 GHz imagery of the turbulent wake from a ship

FACET MODEL USED  
 FACET 6X5 FEET  
 90 GHz  
 DESTROYER AT 15 KNOTS  
 SUMMER ATMOSPHERE



CALM SEA



FULLY DEVELOPED SEA WIND SPEED 12 KNOTS

Fig. 31 -- Modeled 90 GHz imagery of Kelvin wake from a destroyer



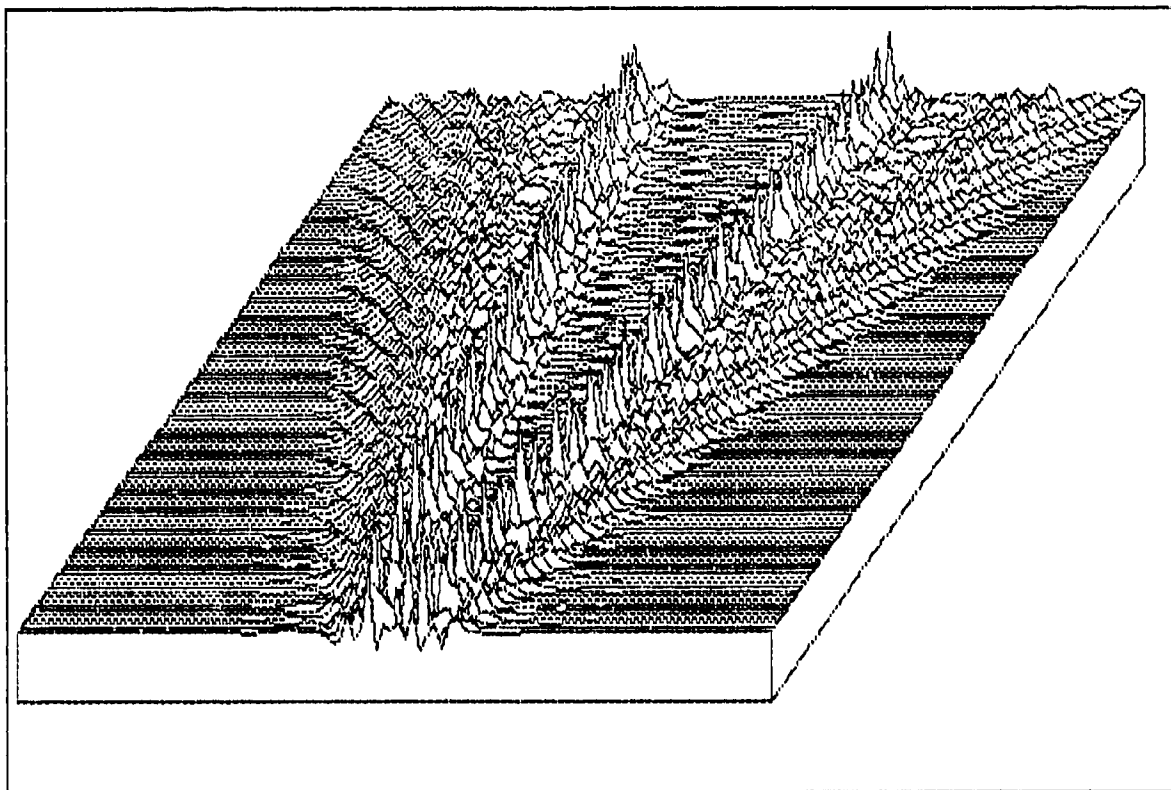


Fig. 32 — Silhouette representation of modeled 90 GHz Kelvin wake from a destroyer

### *Infrastructure*

Masonry structures, industrial and other buildings, road networks, runways, residential areas and other cultural features will often have a high emissivity above that of pasture lands or forests and will appear hotter than surrounding area. Metal roofed buildings, oil tanks, bridges, rail networks and terminals and other structures predominantly metal will have low emissivities and will appear cooler than the surrounding area. Figures 14 and 15 show the effect of high emissivity targets on land such as buildings and roadways. With the structure of roads, railways, and runways extending over many resolution elements, pattern recognition techniques can greatly enhance identification and minimize noise levels. Since these infrastructure targets are stationary, it will be possible to combine a number of passes to eliminate weather effects and enhance the interpretation of these structures.

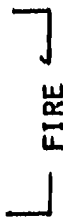
### *Battlefield Damage Assessment*

Smoke is essentially transparent at millimeter wavelengths. This allows especially the 100-m resolution baseline system to be effective in a battlefield damage assessment. The location and extent of fires is readily distinguished through the smoke. An example of this is shown in Fig. 33. The microwave image at 36 GHz clearly delineates the hot burning region of forest fire that is totally obscured in the visible photo shown below it. Because of the much higher temperatures smaller burning regions would be detected. For example, an intense fire has a temperature of as much as 1200 K above the background, and, for an atmospheric loss of  $\alpha \approx 0.2$ , the burning region would require an area of only 16 m<sup>2</sup> to

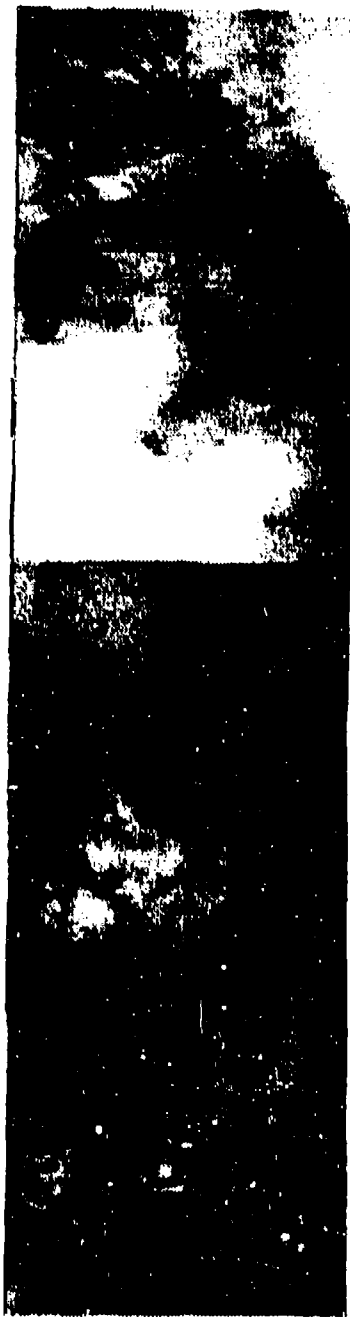
SANTA YNEZ MOUNTAINS FOREST FIRE  
MICROWAVE RADIOMETER MAP



CARPENTERIA



L. JAMESON



AERIAL PHOTO

5000 FT. AGL 8 OCT. 1971

Fig. 33 - 34 GHz imagery of a forest fire

produce a S/N of 6 with the 100-m resolution system. An area of 128 m<sup>2</sup>, i.e., a region with dimensions of about 11 m, would be needed for the 400-m resolution system. Thus individual aircraft, tanks, or vehicles in addition to piers, buildings, and oil storage tanks will be detectable. Furthermore, it should be possible to assess the damage done to runways, roads, and bridges.

### Environmental Signatures

Microwave radiation carries information on the geometric and bulk-dielectric properties of the surface and volume of atmosphere viewed. The intensity of upwelling microwave radiation from the environment is a function of frequency, polarization, incidence angle of observation, emissivity of the scene, and transmission through, and radiation by, the atmosphere. At 90 GHz, the microwave sensor is sensitive to many atmospheric phenomena of interest, as well as surface phenomena, which must be discriminated or analyzed together for a particular scene. For convenience, surface and atmospheric signatures are discussed separately.

### Surface Signatures

Environmental targets are categorized as localized surface features; they range from a percentage of beam-fill to many beams in size. For example, oil spills on the sea have the effect of smoothing the surface and reducing foam, thereby decreasing effective temperature. Over large areas this will appear as a parcel of below normal temperature, and it would be relatively easy to map the spill's extent. At thicker portions of a spill, the surface layer becomes significant compared to the wavelength of the detected signal, and interference effects can change the perceived signal to a positive level. For another example, snow and ice cover are targets of large area that can be mapped easily. In addition, ice types, first year and multiyear, can be discriminated, and snow signature will vary with liquid water content. The 100- to 400-m resolutions can find openings in ice packs and trails in the ice made by ships. Thin first-year ice can be located and sized for ship traffic. With 400-m or better resolution, icebergs can be located and tracked. For agriculture, soil moisture variations over relatively small areas can be located and vegetation stress estimated for crop yield and disease control. Soil/vegetation composites can be measured. Fires and slash-and-burn areas can be located and time histories generated. Surface moisture can be measured to indicate the effects of localized flooding and estimate the condition of the soil for vehicle movement. Soil texture can be observed for volcanic or recent man-made activity. Figure 34 shows broad categories of surface types that currently are distinguishable at 12.5-km resolution for frequencies near 90 GHz that can be observed as background for targets. Table 2 shows characteristics, including emissivities, of surface environmental targets.

### Oil Spills

Oil on the sea surface damps out the short millimeter capillary waves that produce increased millimeter-wavelength radiation. This results in the area of the sea covered by the oil slick appearing cooler than the adjacent unpolluted sea. The presence of oil also greatly suppresses the production of sea foam, which also results in a reduction of the millimeter-wavelength signal in the slick. The oil tends to be driven into thick pools at the downwind edge of the slick. The majority of the area of the slick is very thin, only a few molecules thick. If the oil thickness is an appreciable fraction of the observational



Fig. 34 — SSM/I land surface types

wavelength in the oil, it will result in an increase in the radiation. The maximum increase occurs for thicknesses of multiples of a quarter wavelength, about 0.5 mm at 90 GHz. This occurs because the oil has a dielectric constant intermediate between the sea and free space. It acts as a quarter-wave matching layer, greatly reducing the sea reflectivity and, thus, increasing its emissivity. Therefore, an oil spill will appear as a cool depression in the millimeter-wavelength radiation over the slick area, with the warm spots where the oil is thicker than a few hundred microns. Under high sea state conditions, the slick will, of course, be broken up and the rough sea and white caps and spray will mask the effects of the oil.

Figure 35 is an image of an oil spill at 22 GHz; the spill region is at the top, the 22 GHz region is in the middle, and the false color bar is at the bottom. The red regions are the higher brightness temperatures from the rougher unpolluted sea. The smoothed region of the slick appears as a cooler blue. The area of the slick is not discernible in the photo as it appears here, but it is on the original negative. The bright yellow spot at the downwind end of the slick is the increased radiation due to a thick, 0.6-mm region of oil. The stern of a ship making surface measurements is visible at the bottom left of the image.

The baseline system will easily map and track oil spills of dimensions greater than 100 m. In the case of large spills, such as those in the Persian Gulf during Operation Desert Storm, it would be possible to infer the thickness and, hence, the volume of oil present. The location and track of the spill could be determined and the largest concentrations of oil could be located, allowing the most efficient containment and clean up measures to be taken. The detection and quantification of oil spills on the land surface has not been investigated in detail, but rough calculations indicate that they should be measurable.

### Bare Soil

Figure 36 shows brightness temperatures observed for a range of soil types and soil/vegetation composites for the Western coast of Africa. The variations in brightness temperatures are caused by differing types of soil, including texture, amount of soil moisture, and vegetation. The brightest (whitest) regions toward the north are the great sand dunes, such as Azefal Dunes and Akchar. The grey-white colors represent the rocky, sandy soil and mountainous regions of the Sahara Desert. A sand storm is blowing out to sea near the coastal city of Nouakchott, coloring the oceanic background turquoise. The brown-white region immediately southeast of Nouakchott represents mixed dry and arable land in the transition region between desert and forest. The brown-green along the southern coast identifies the Ivory Coast, a composite of arable land and forest. The darkest green identifies the lush forested region of the Niger Delta. The white patterns over the sea and land to the south are clouds and humid air. The small, turquoise and yellow regions within the white clouds are cumulonimbus convection.

Normal, dry soil has an emissivity of 0.90 to 0.95 at microwave frequencies, so that its apparent temperature is close to its physical temperature. The emissivity of dry soil is nearly constant with frequency, so that the apparent temperatures at 90 GHz would be similar to those at SSM/I (sensor system microwave/imager) frequencies, except that atmospheric clutter may be somewhat greater at the higher frequency. With 100- to 400-m resolution however, it is a tractable problem to separate the spatial and temporal frequencies of land and atmosphere in the imagery; a problem that is much more difficult at SSM/I resolutions. This would allow greatly improved target identification over land, compared to SSM/I capabilities. Also, emission from dry soil is fairly highly polarized; the vertically polarized brightness

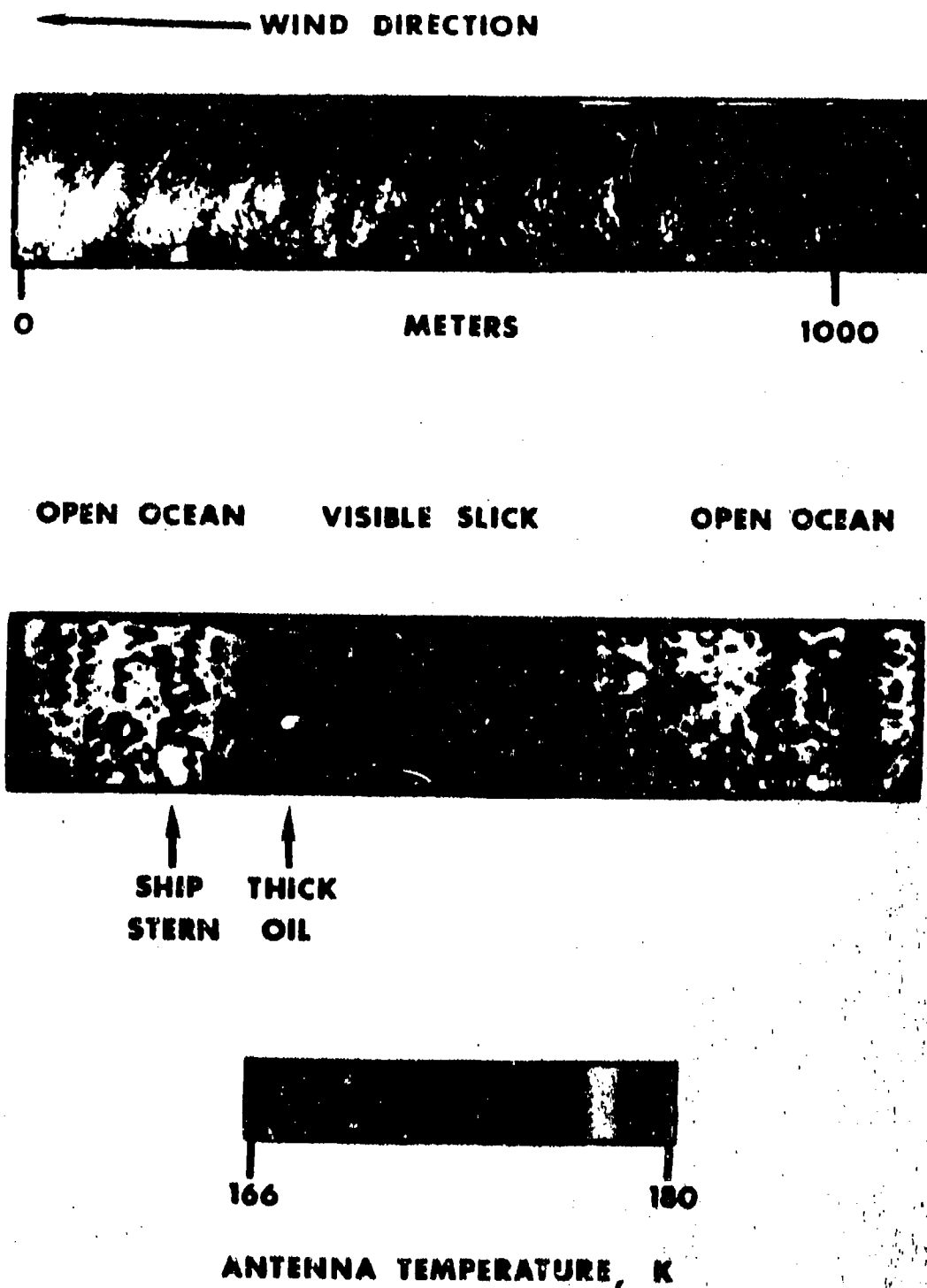


Fig. 35 - 22 GHz imagery of an oil spill



Fig. 37 — SSM/I 85H image of a weather front over southeastern United States

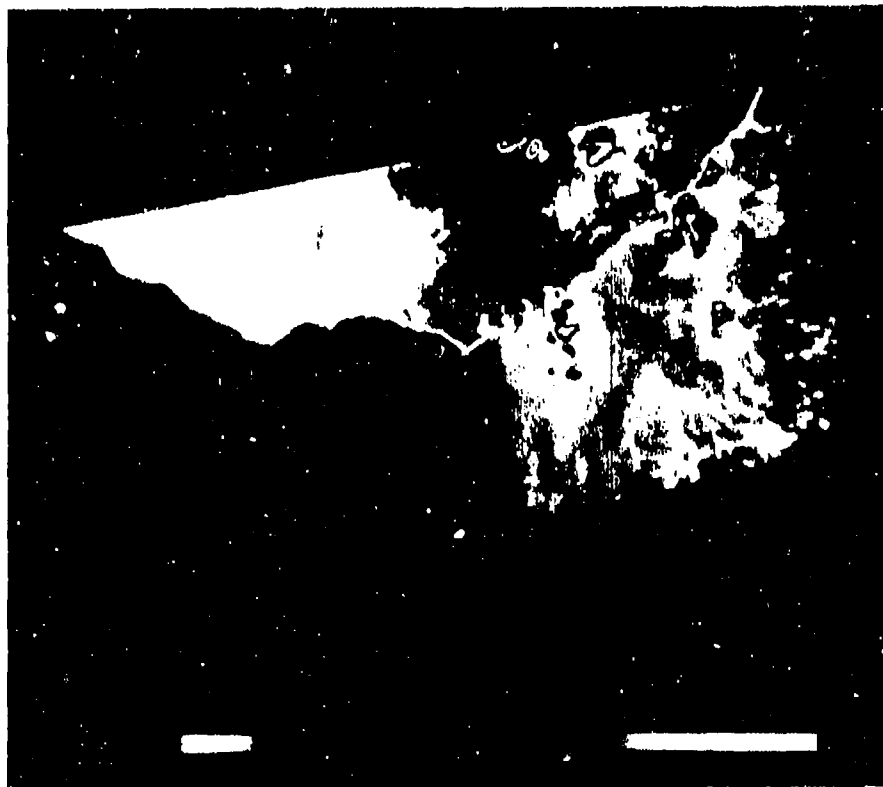


Fig. 36 — SSM/I 85H image of African soil and vegetation types

is greater than the horizontally polarized brightness. At SSM/I incidence angles, the polarization difference can exceed 50 K. Atmospheric features are much less polarized than for land, so that the identification of clutter is aided.

Adding water to dry soil dramatically changes its radiative characteristics and appearance in microwave imagery, as shown in Fig. 37. The color bar ranges from 150 to 300 K. Land has been saturated white for atmospherically clear regions. A cover of thick nimbostratus and cumulus clouds is moving across the southeastern United States, accompanied by light rain. Approximately 80 to 90% of the surface radiation is transmitted through the clouds and reveals wet ground conditions. The contrast for every river and lake is increased dramatically, including the extensive run-off of the Mississippi River valley. No surface features are showing in the normally dry, white areas. Thoroughly moistened soil has an emissivity of 0.7 or less, and thus significantly lower brightness temperatures than the same soil in a dry condition. The decrease in brightness temperatures after light-to-moderate rains can be as much as 40 to 50 K. As soil moisture increases, the difference in polarization increases as well, from about 50 K for dry ground to 70 to 80 K for thoroughly wet soil. The amount of soil moisture, therefore, can be determined.

Changes in soil moisture can be observed through vegetative canopies of all kinds. The decrease in brightness temperatures observed after rains in the Carolinas is about 10 to 15 (Fig. 38) The left side of this figure is an SSM/I 85H image of the eastern seaboard on 30 August 1989, 20 days before Hurricane Hugo arrived. The swath extends from Florida to the Delmarva peninsula. The color bar is the same for both left and right images. The greens and browns identify low-altitude terrain, green representing the highest brightness temperatures. "White" identifies primarily clouds but also high-altitude terrain, such as the tops of the Appalachian mountains. Blue identifies the ocean, Lakes Marion and Moultrie north of Charleston, South Carolina, and also the deeply convective regions of clouds where precipitation is expected. The remaining colors (turquoise, gray, and yellow) identify the increasingly deeper convective regions within storms where backscattering hydrometeors are present. Except for widely scattered thunderstorm activity near the Appalachian regions, the eastern U.S. is clear. The emissivity of the terrain for a given land type is proportional, not only to land temperature, but also to the density of live vegetation, and is inversely proportional to the amount of surface groundwater. Note the dark green expanse throughout the Carolinas. The image on the right depicts the eastern seaboard on 23 September 1989, within two days after landfall. The scene north of Florida and east of the Appalachian mountains is free of clouds. (The four thin, black arcs across this region indicate data drop-outs.) The average brightness temperature in the vicinity of the Chesapeake Bay is approximately the same as that in the left image; in the pathway of Hugo, however, the average brightness temperature has decreased. This can be interpreted primarily as an effect of increased groundwater in the soil/vegetation composite. It is possible that part of the decrease in brightness temperature is caused by massive defoliation. Observe also the differences for Lakes Marion and Moultrie; the increase in groundwater is evident.

Observations with the 85.5 GHz channel of the SSM/I have shown that it is possible to identify high-contrast features of terrain, such as wet-land-dry-land boundaries of rivers and lakes. This is possible even when the sensor's beam size at the surface is greater than about 5 to 10 times the width of the feature, depending on the amount of moisture, the size of the feature, particularly when the two-dimensional feature is unresolved in one direction only. It should be possible, therefore, at 100- to 400- m resolution to see the wet condition of features as small as roadways, streams, bogs, topographical drainage, and pollution patterns. For example, since the spatial frequencies of significant mountain and natural drainage topography range from about 100 m to about 1 km, complete topographical maps of soil moisture could be made for hydrological and military purposes.

Another effect to be considered in observing soil with microwaves is the roughness of the surface. It has been observed that the emissivity of rough soil is slightly greater than that of smooth ground. A freshly plowed tract or an unpaved roadway roughened by passage of heavy military vehicles, for example, should appear slightly brighter in microwave imagery than smoother ground. Another example is the measurement of volcanic lava flow morphology and topography. Recent investigations of lava flows [1] have shown that spatial variations in the surface textures on lava flows can be identified from Space Shuttle radar images. This demonstrates the potential for remote sensing at millimeter wavelengths to map the distribution of different kinds of lava over an entire volcano. The potential exists, at 100- to 400-m resolution, for measuring flow position and volume during eruptions, even under cloud cover, for prediction or other purposes. Orbiting platforms could be used to detect the rate of change of volcanic landforms such as domes, cones, and calderas by frequently imaging the volcano with a high-resolution microwave system.

### Vegetation

The appearance of vegetation in microwave imagery (as in Figs. 36-38) is a combination of modified radiation from the underlying soil and emissions from the vegetative canopy itself. Both of these processes depend on the optical thickness of the vegetation or biomass present. Plants can be described as aggregates of cell-sized liquid water and fibrous structures that absorb and scatter radiation from the soil below. Also, plants are very good emitters, having emissivities 0.80 - 0.95. The soil beneath significant amounts of vegetation usually is moist, so that (for nearly equal thermometric temperatures) the higher emissivity of vegetation determines higher brightness temperatures. Vegetation, therefore, appears warmer than the surrounding moist ground by an amount that depends on the type of vegetation. Another property of the radiation emitted by vegetation is that it is unpolarized. To the extent that the plant's absorption and scattering attenuates the soil's radiation, the signal from the soil/vegetation composite will have a lower polarization difference, which approaches zero for a lush rainforest. The microwave sensor thus is capable of distinguishing the amount of vegetative cover. In addition, Ref. 2 shows that metal/vegetation composites have emissivities significantly less than those of soil/vegetation composites. Orbiting high-resolution microwave sensors would be capable, for example, of distinguishing nonvegetative military camouflage from true vegetative canopies or of detecting large masses of military equipment beneath trees. Also, man-made clearings could be distinguished from river tributaries, and deforestation caused by cutting and burning could be monitored. The slash-and-burn conversion of forests can lead to higher concentration of greenhouse gases, large aerosol concentration, and smoke-like layers over the burning regions, increased surface albedo and water run-off, and a decrease in evapo-transpiration—all leading to undesirable environmental and climatic changes.

Plant diseases or drought create vegetative stress and have significant negative effects on its emissions. For example, as vegetative moisture decreases, the emission, absorption, and scattering of the plants also decrease, and the effects on radiation from the soil are reduced. The emissivities of stressed vegetation usually drop to about 0.87 or less. As the biomass dies, the radiometric effect is similar to increased soil roughness; polarization of radiation is higher for unhealthy plants. A high-resolution microwave imager would be capable of monitoring the vegetative stress of diseased forests or croplands on a scale of a few hundred meters, during the incipient stage before irreversibility to good health occurs. Damage assessments would be possible for these areas and also for regions of significant wind damage, as shown in Fig. 38.

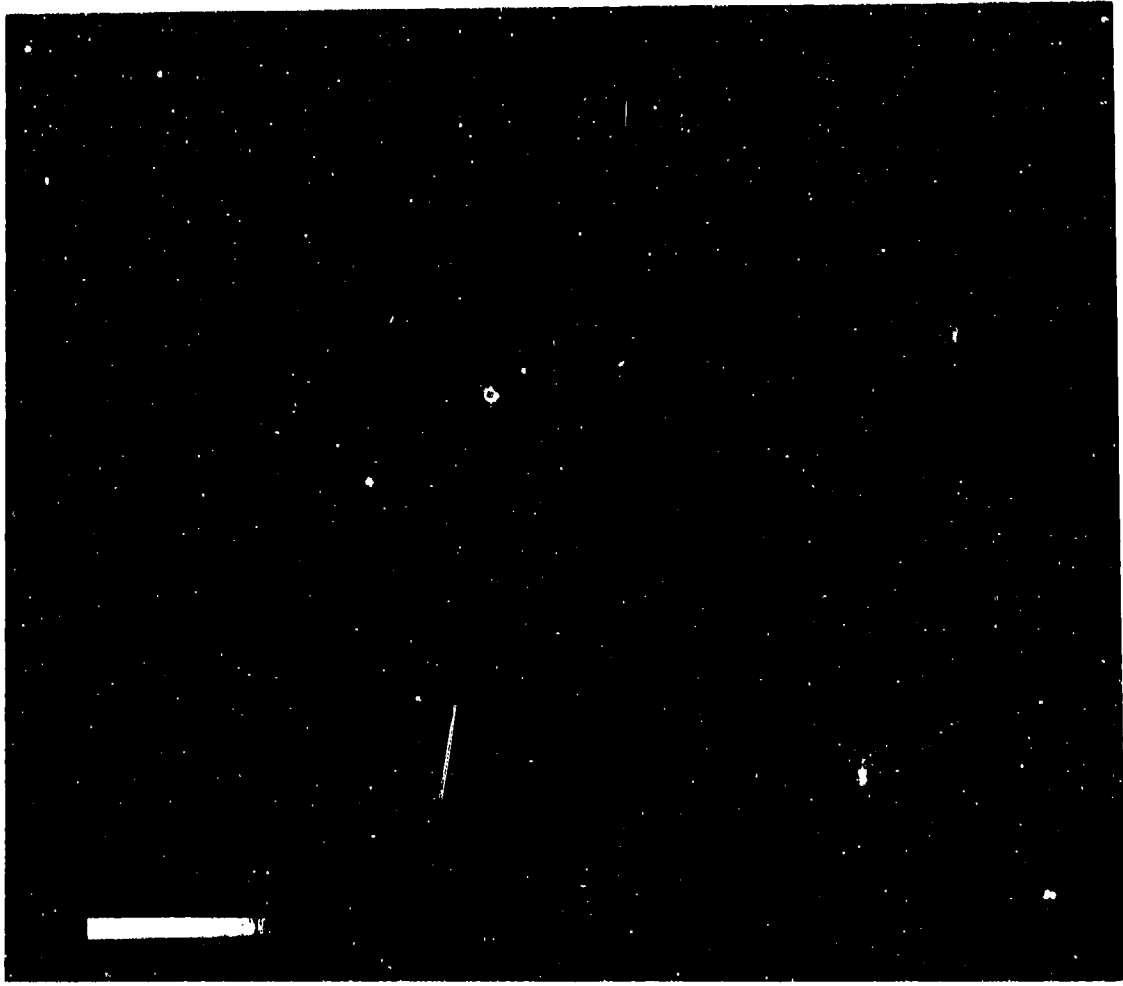


Fig. 39 — SSM/I 85H image of snow in the Midwest

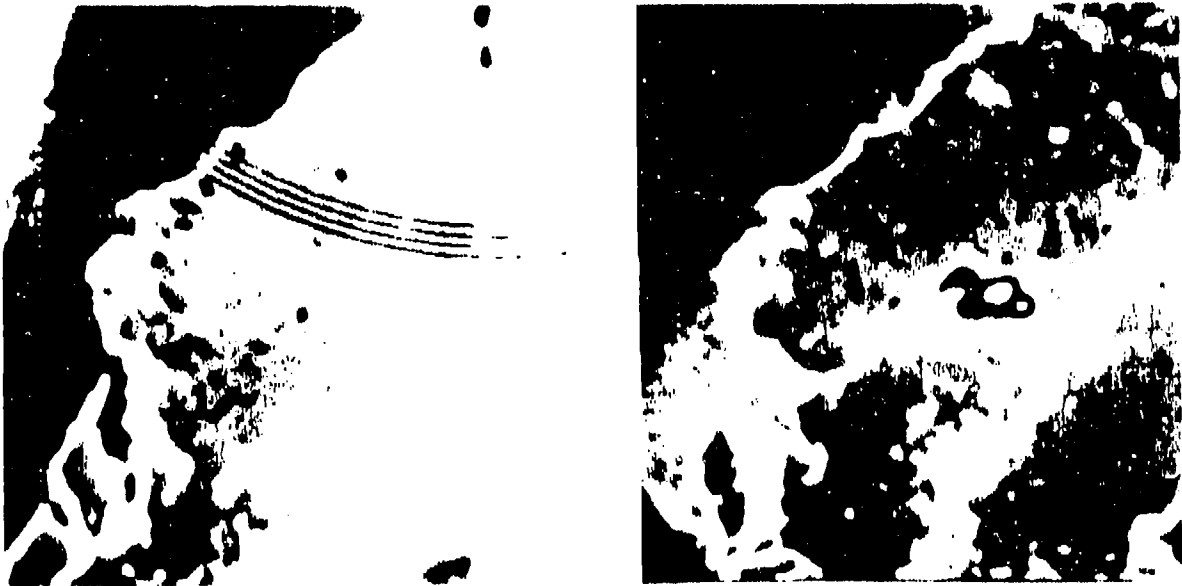


Fig. 38 — Eastern seaboard before and after Hurricane Hugo

## Snow Cover

The microwave response to snow is complex and quite different from that to ice or water, because snow has varying amounts of air, water, and ice in it over a varying background of soil. Basically, the primary effect of dry snow at the higher microwave frequencies above 20 GHz, besides reducing the polarization difference of the radiation from the underlying soil, is to scatter radiation from below, since the snow particulates and air pockets are of the order of the size of the wavelengths. The scattering asymptotically approaches a maximum value as depth increases, so that the brightness temperature decreases. Snow is much colder radiometrically than bare soil, and becomes colder as snow depth increases. The effect increases with microwave frequency, but so also does clutter from clouds and rain when present. The current advantage of a microwave sensor, therefore, exists in the absence of rainfall. Figure 39 shows an SSM/I image of snow at 85.5 GHz on a relatively clear day, with the color bar ranging from 150 to 300 K. Normal snow-free, local variations in 85GHz brightness temperatures of U.S. land rarely exceed approximately 15 K for a given amount of soil moisture. Following this midwinter snow storm in the Great Lakes region in 1988, the surface variations, red to green, increased to as much as 50 K in the midwest. The green belt south of Lake Michigan represents several inches of snowfall. The orange spot in Lake Superior is Isle Royale.

The microwave response changes dramatically when the snow becomes wet. Water in the snowpack increases the composite's extinction of radiation from the soil by absorption and decreases extinction due to scattering. When wet, therefore, the composite approaches the nonscattering condition characteristic of a blackbody radiator. Wet snow, consequently, is radiometrically warmer than dry snow, as well as having a higher polarization difference because of the greater discontinuity between water and air.

As a snowpack melts and refreezes repeatedly and becomes more densely packed, it scatters radiation from the ground more efficiently. The age of the snowpack, therefore, will be associated with distinctly different ranges of brightness temperatures (Fig. 40). The average spectra for brightness temperatures  $T_b$  have been observed [3] at horizontal  $H$  and vertical  $V$  polarizations for

- winter-snow conditions, with the snow depths for all measurements normalized to a 48-cm water equivalent, and for each of two spring-snow conditions;
- a wet firm layer at least several centimeters thick on the surface of the snow cover; and
- a thick crust, at least several centimeters, of refrozen firm.

For dry snow, an increase in frequency is accompanied by an increase in both the extinction coefficient and the albedo. The result is that, for a given depth of snow, or water equivalent,  $T_b$  decreases with frequency. The two sets of spectra are obviously different in two respects, however:

- the polarization difference  $T_b(V) - T_b(H)$  is much larger for winter snow than for spring snow; and
- the  $T_b$  of dry spring snow decreases faster with increasing frequency than the  $T_b$  of winter snow.

These differences are attributed to differences in the shapes and sizes of the ice crystals characteristic of the two conditions. The stronger polarization dependence of winter snow is caused by the asphericity of new snow crystals; however, they become more spherical after several cycles of melting and freezing. This is a characteristic attribute of spring snow. The melting and refreezing process also produces larger crystals, because the snow crystals tend to combine with each other. This, in turn, leads to more scattering or a larger albedo and is responsible for the stronger dependence of spring snow on frequency. At 90 GHz, the dynamic range of brightness temperatures for these differing snow types is of the order of 100 K.

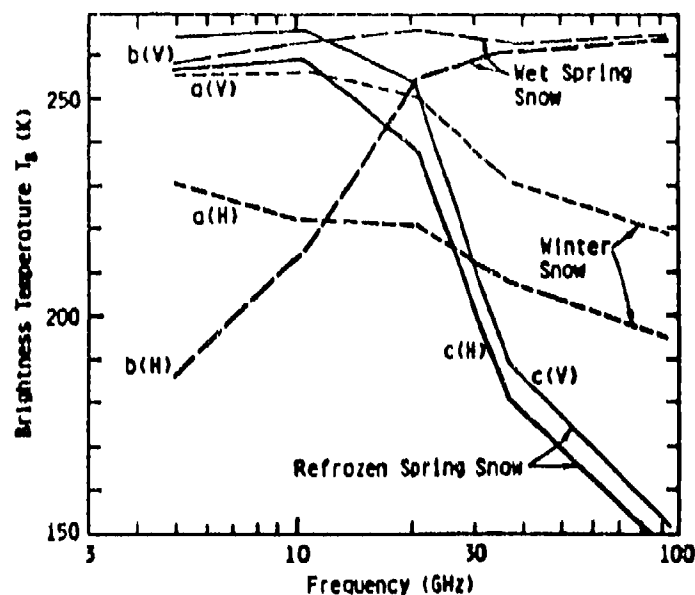


Fig. 40 — Frequency dependence of brightness temperatures for snow types

The appearance of snow undergoing significant melting is difficult to distinguish radiometrically from extremely wet soil. Previously, the only reliable way to identify the two cases has been a temporal approach to the snow-melt history of the area. High-resolution radiometry, however, may provide the additional aid of imagery of the local topography and morphology of snow-melt run-off.

An example of the contribution a high-resolution 90 GHz sensor could make in environmental monitoring is in the prediction of volcanic activity. Periodic mapping of the summit areas of volcanoes to determine the amount of snow cover, the temperature of a summit lake in the absence of snow, or the extent of fumarole activity within a snowpack would all be of value in monitoring the onset of new activity.

### Water and Sea Ice

The emissivity of different targets is a consequence of their dielectric properties. Since water is a polar molecule, it has a very large dielectric constant at microwave frequencies, which implies a large reflectivity and low emissivity for a liquid water surface like the ocean. Most natural solid surfaces have emissivities in the 0.88 to 0.95 range, so there is a significant contrast between liquid water surfaces, such as lakes, rivers, and the oceans (whose emissivities are about 0.6 - 0.7 at 90 GHz, depending on windspeed and climatic zone) and solid surfaces, such as land or sea ice. The effects of salinity and sea surface temperature are negligible at 90 GHz. The low emissivity and homogeneity of the open ocean make it a good background for viewing the intervening atmosphere. At 100-400-m resolution, large lakes and rivers and inland seas, such as the Red Sea, also would be resolved, and, by contrast, ponds 25 to 100 m wide or less could be detected. Within the boundaries of larger bodies of water, atmospheric clutter and pollution could be monitored, for example, and used as a reference or baseline for nearby atmospheric clutter over land; the smaller bodies of water could be monitored, at least, for varying water-fill for hydrological and meteorological purposes or for pollution. Surface ice edge within the larger inland water bodies could be measured, and small icebergs on the open sea could be monitored for traffic and research.

Sea ice is observed unambiguously in four radiometric categories:

- newly formed (young) ice with thickness up to 30 cm;
- first-year ice (FY), which has yet to go through the annual process in which the upper layers melt and refreeze, with thickness between 30 cm and 1.2 m;
- second-year ice (SY), with thickness 1.2 to 2.5 m; and
- multiyear ice (MY), with thickness greater than 2.5 m, which has undergone at least one melt cycle.

Sometimes young ice will be grouped with FY ice, SY ice with MY ice. The inherent distribution of emissivities of all ice types is sufficiently well separated to allow each ice type to be easily distinguished by its microwave signal, as will be shown below.

The higher salinity of FY ice causes it to be optically opaque, and, therefore, its microwave signature is almost frequency independent (Fig. 41) [4]. In contrast, the emissivity of MY ice decreases rapidly with frequency to a minimum near 90 GHz [5]. The virtually desalinated outer portion of MY ice makes it optically thin since the radiation emanates from a thicker layer of old ice. A significant fraction of the radiation from old ice is suppressed by volumetric scattering within the ice because of air pockets formed during summer melt and brine drainage. The emissivity of MY ice, about 0.6 to 0.7, is lower, therefore, than that of FY ice.

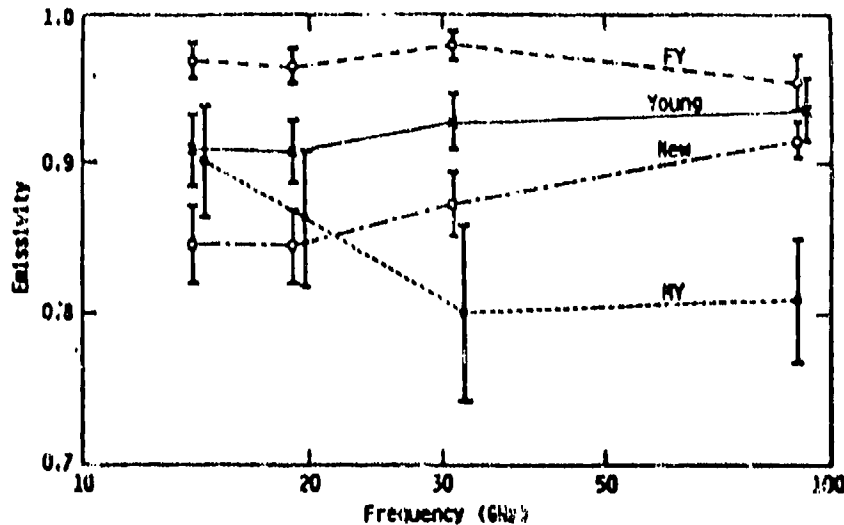


Fig. 41 — Frequency dependence of emissivity for sea ice types

The great difference in emissivity between FY ice and MY ice at the higher frequencies would lead to greater information content, because of greater contrast, in the imagery of an ice field, including observations of new ice parcels less than the instrumental resolution appearing in an old field. The situation in a melting or broken ice field is more complex but amenable to analysis. Figure 42 is a radiometric image of mixed fields of Arctic sea ice observed at 90 GHz from aircraft, showing the contrast between FY ice (blue) and MY ice (red). An analysis of imagery of this kind has yielded the population distribution vs temperature of ice types and open water in the Beaufort Sea in July 1983 (Fig. 43). Each curve is derived from an individual ice floe and from a single continuous area. Values

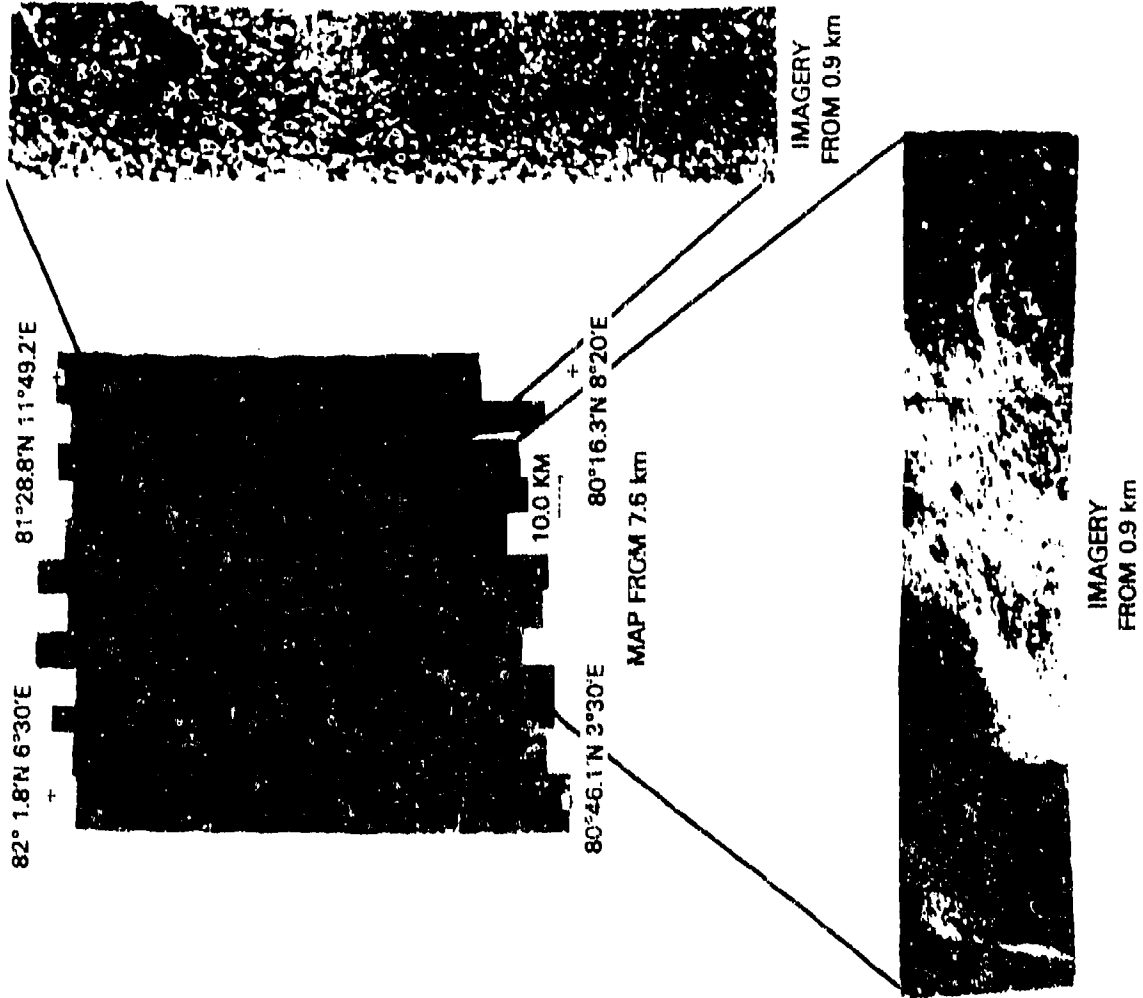
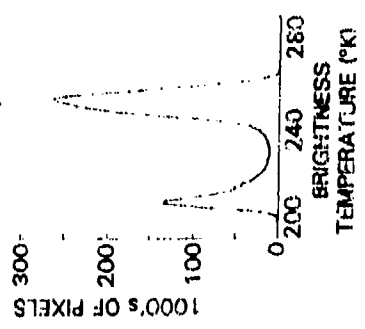


Fig. 42 — 90 GHz imagery of arctic sea ice



AVHRR SATELLITE INFRARED IMAGE  
(RECTANGLE INDICATES MAP AREA)

90 GHz  
 JULY 1, 1983  
 HIGH ALTITUDE MAP  
 $T_w = 206.4^\circ\text{K}$   
 $T_i = 252.8^\circ\text{K}$



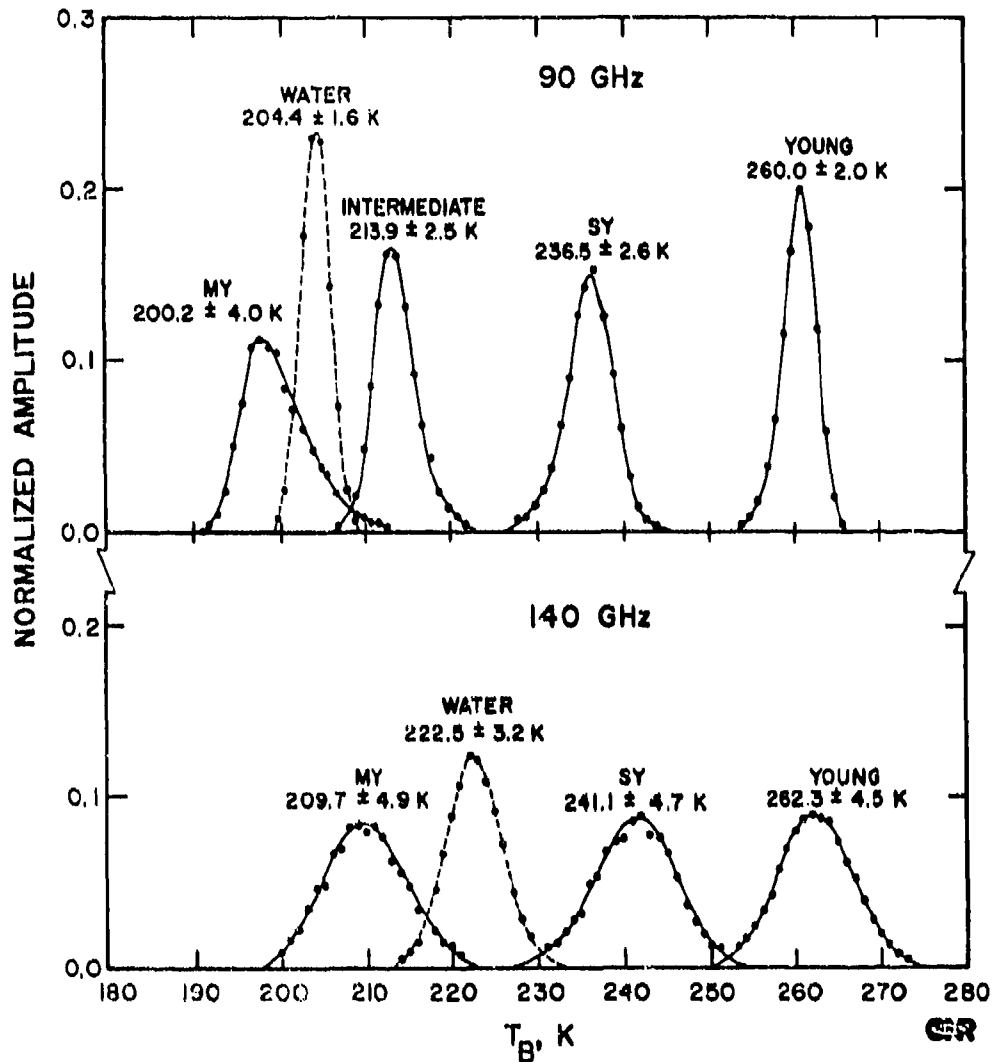


Fig. 43 -- Brightness distribution of sea ice types at 90 and 140 GHz

of the mean and standard deviation are given. The standard deviation for open water, a homogeneous microwave scene, is approximately equal to the instrumental noise of 1.4 K at 90 GHz. Thus a significant portion of the spread in the microwave signal for a single ice type is due to instrumental noise. The broadening as a result of instrumental noise may be removed to obtain the standard deviation in the ice  $T_b$  at 90 GHz, alone of 1.4 K for young ice, 2.2 for SY ice, and 3.7 for MY ice. The inherent distribution of emissivities for all ice types thus is well separated.

MY ice may appear radiometrically colder than the sea. Because the sensitivity to volumetric scattering is inversely related to the wavelength of the radiation, a greater variability in the brightness distribution of MY ice would be observed at 90 GHz than at lower frequencies. This distribution overlaps that of open water (Fig. 43). In those cases where the emissivities of MY ice and open water are the same, it is possible, nevertheless, to distinguish ice from water. The difference in polarization for ice is less than that for water because of the difference in volumetric scattering.

The emissivities of FY ice at 90 GHz are 0.92 and 0.96 without and with snow cover, respectively (Fig. 44) [4]. The presence of snow on the ice increases the emissivity because the snow provides a smoother transition in the dielectric properties between ice and air, and hence a better impedance match, and also because it insulates the ice from the lower temperatures of the air.

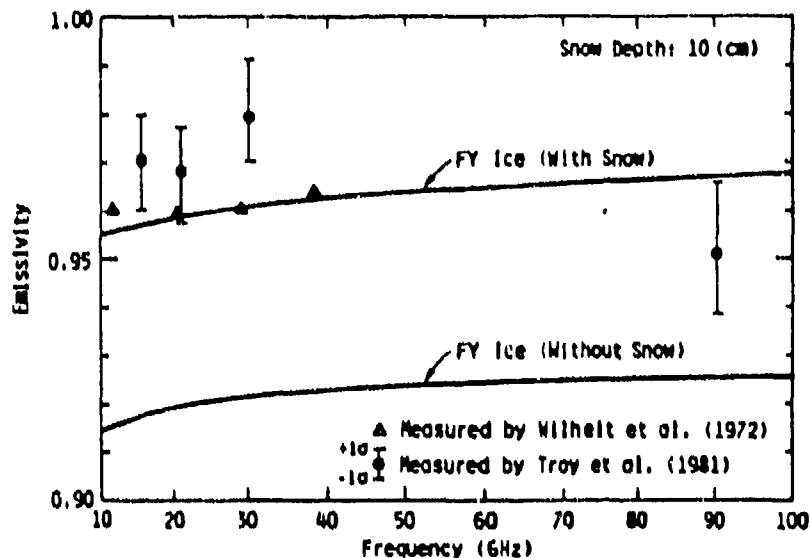


Fig. 44 — Emissivities of FY sea ice with and without snow cover

High resolution, 90-GHz radiometry also will detect small icebergs, floes, and fractures, as well as ages and concentration, in all weather, on a scale less than currently measured with infrared (IR) sensors. Arctic and Antarctic regions are cloud covered much of the time, so that all-weather capability is particularly important. At 100- to 400-m resolution, an orbiting microwave sensor would have the capability of guiding a ship through ice fractures at night or beneath heavy cloud cover. The sensor could also provide predictive capability for ice breakage by sensing the boundaries between fresh ice and shelf ice—sites of frequent ice breaks. In another case, large icebergs, such as Antarctica's B-9 of 1987, tend to break from fractures in shelf ice itself because of interference from covered islands or flows of under-ice water current. These fractures are preceded by much thinner depths of connecting ice and would likely be identified because of anomalous variations of emissivity in MY ice, consistent with the pattern of fractures.

### Atmospheric Signatures

The atmosphere is neither perfectly transparent, emissivity = 0, nor opaque, emissivity = 1, to microwave radiation upwelling from the surface. It varies locally between the two extremes, depending on atmospheric conditions and frequency, opacity increasing with frequency. For this reason, many weather features, as seen in the global 85H image of Fig. 45, can be observed and measured by microwave radiometry. The primary atmospheric constituents that affect the radiative transfer of microwaves at 90 GHz are cloud drops, rain drops, graupel particles, ice crystals, aggregates including aerosols, and the molecular gases of water vapor and oxygen. For example, Table 3 lists typical relative contributions in percent, of the atmospheric constituents to the upwelling radiation in a thunderstorm [6] and compares them with clear sky conditions. The concentration of these constituents along the line of

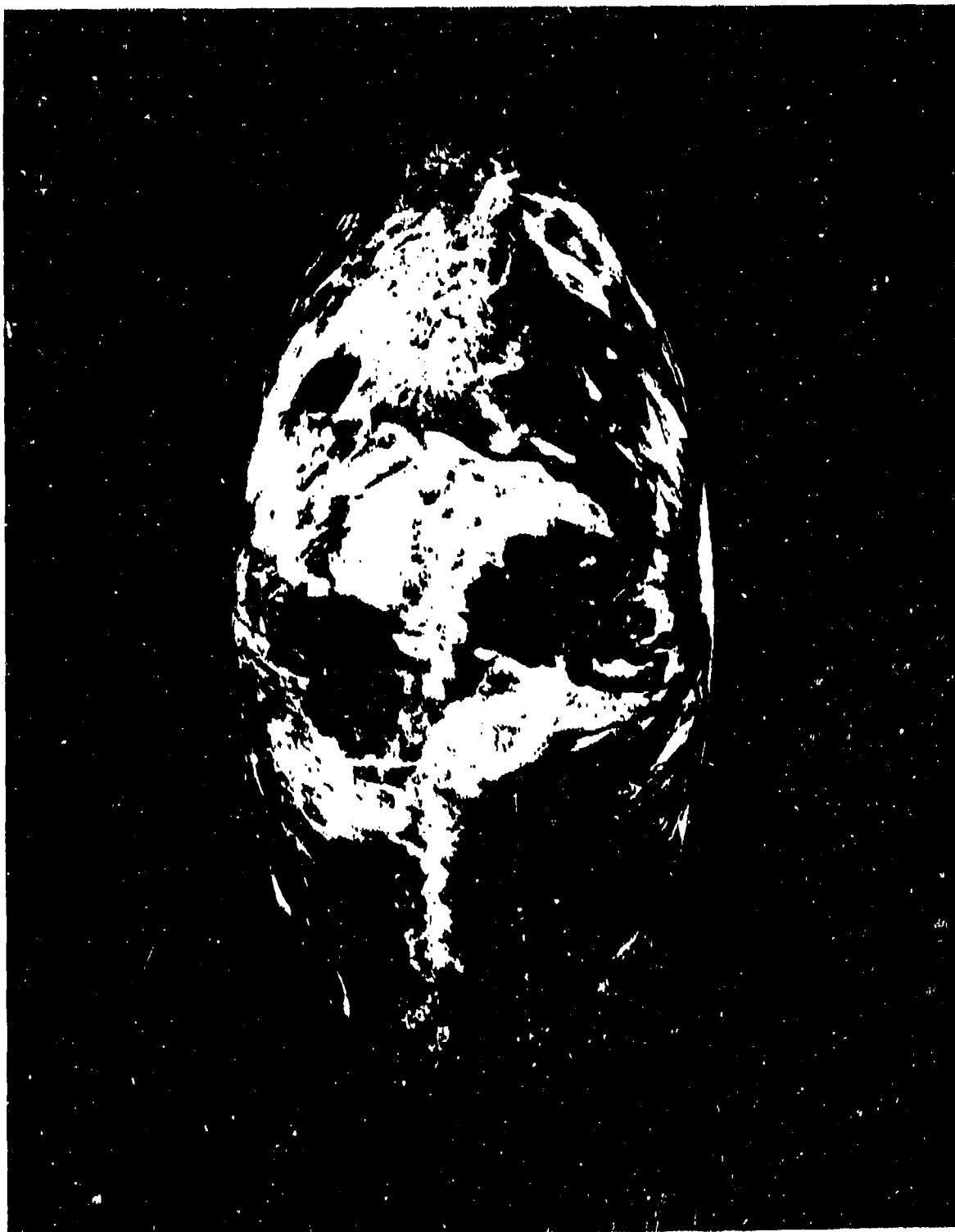


Fig. 45 — Microwave image of the world at 85.5 GHz

sight determines the absorptive, scattering, and emissive profile of the atmospheric source function. The table illustrates the range of possible contributions to the source function. The columnar integration of the source function determines the effective emissivity of an atmospheric feature. Table 4 lists the measured emissivities of various atmospheric features observed in 85.5 GHz SSM/I images, and Table 5 gives the environmental loss at 90 GHz for radiative transmission.

### Clouds, Rain, and Water Vapor

The relative contributions of atmospheric features and land are typical in the microwave image of the world (Fig. 45). The coolest parts of the globe are the ice of Antarctica and the Greenland plateau. Ice packs of the polar seas and ice of the continental shelf are brighter than the sea. The warmest and brightest parts of the globe are low-altitude land. Mountains, lakes, and rivers such as the Amazon, are darker, cooler features on the continents. Clouds vary greatly in brightness, depending on the amount of water present. The clouds over the equatorial region are primarily of the cumulus family; those at high latitudes are primarily stratus clouds. Rain and hail in thunderclouds backscatter radiation from below so that regions of precipitation are relatively dark, as in the spiral rain bands of Hurricane Gilbert in the Gulf of Mexico. Slow variations in the blue background are due primarily to atmospheric water vapor and small amounts of cloud liquid water.

Most atmospheric features, such as those in Tables 4 and 5 are associated with cloud signatures. A cloud is an aggregate of hydrometeors produced by a proper distribution of hygroscopic nuclei, a sufficient amount of water vapor, and proper dynamics or convective motion that raises parcels or layers to their lifting level for condensation. For 90 GHz imagery, clouds can be divided into two broad categories by altitude and composition. The first category contains the high-altitude cirrus clouds made of small ice crystals. Cirrus clouds are optically very thin at 90 GHz and at SSM/I frequencies and are virtually invisible. This property can be a significant advantage when observing storm systems, which often have a cirrus shield that prevents the use of IR and visible data for analyzing the underlying structure of the system. A microwave imager does not see the shield, so that the location of cumulonimbus and other thick clouds, rain cells, hail, graupel, dust, and convergent winds can be determined, as in Fig. 45 (explained below). The other species of ice or ice aggregates, such as hail and graupel, found in lower-to-mid-altitude clouds, the second category, appear somewhat like rain to the SSM/I, but scatter even more radiation.

Figures 46 and 47 present a comparison of visual and microwave imagery of Typhoon Sperry. Typhoon Sperry, partially seen in visible light at local sunset time near the Philippines on 29 June 1987, is shown at maturity. The core of the storm, as well as thunderclouds outside the gale envelope, and the island of Mindanao (lower left), as seen in Fig. 47, are veiled by the dense overlying cirrus clouds at 50,000 ft. To the east (right) in the visual image, much of the lower atmosphere is hidden in the darkness behind the setting sun. The SSM/I senses the scene below 50,000 ft and produces a detailed 85H microwave image of the eye and eyewall of the typhoon, Mindanao (white) in the southwest, and the band of thunderclouds streaming from the direction of Mindanao toward the southeastern flank of the typhoon. The brighter-colored parts of the thunderclouds are deeply convective regions containing rain and hail. The darker outside regions indicate precipitation that is likely to be mostly rain. The SSM/I also permits a view of the lower level clouds and windstreaming in the darkness to the east. In the upper right and left corners of the image (Fig. 47), frontal lines separate the humid cyclonic air from the drier, high-pressure regions through which the typhoon is passing.

The second category of clouds includes cumulus, stratus, and their variational types and is composed primarily of water droplets. The total extinction by absorption and scattering of upwelling radiation from



Fig. 46 — OLS visual image of Typhoon Sperry

the land/ocean surface caused by these droplets increases with the thickness and water content of the cloud. The zenith attenuation ranges from approximately 0.1 dB for stratus clouds, to approximately 1.5 dB for cumulus, and greater than 5 dB for cumulus congestus clouds. The clouds of greatest optical thickness (Table 3) are opaque to almost all radiation from the surface, whereas, for example, stratus clouds transmit much of the radiation, as shown in Fig. 48. The look-up table for the color bar, 150 to 300 K, is based on histograms and atmospheric models of cloud-free and cloudy ocean regions, and the image has been enhanced for cloud signatures. The cloud-free tropical ocean is radiometrically colder than land (white) and provides a slowly varying blue background. Land has been saturated white so that the more significant clouds over land could be seen as a blue mottling against the brighter background, with minimal confusion from the details of land. A cover of stratus and stratocumulus clouds, identified as turquoise and purple over the ocean, is moving across the Baja Peninsula. Approximately 90% of the upwelling 85.5 GHz radiation from the surface is transmitted through these clouds, which almost completely blocks visual radiation. To the south, white cumulus clouds circulate around a tropical low preceding Hurricane Hilary 1987; the darker colors in the core identify deeply convective cumulonimbus clouds, the only clouds in the image, that significantly attenuate microwave radiation.

The opacity of clouds increases with cloud liquid water content and microwave frequency, since absorption and scattering increase with frequency. It has been determined from preliminary SSM/I observations of surface signals at 85.5 GHz that clouds with cloud liquid water content greater than approximately 0.4 to 0.5 kg/m<sup>2</sup> severely attenuate signals from below. Figure 49 shows a latitudinal distribution of these nearly opaque microwave clouds for a week in October 1988. The 85H data used to produce Fig. 50 were gridded and averaged over 4-deg sections in the same manner as the previously

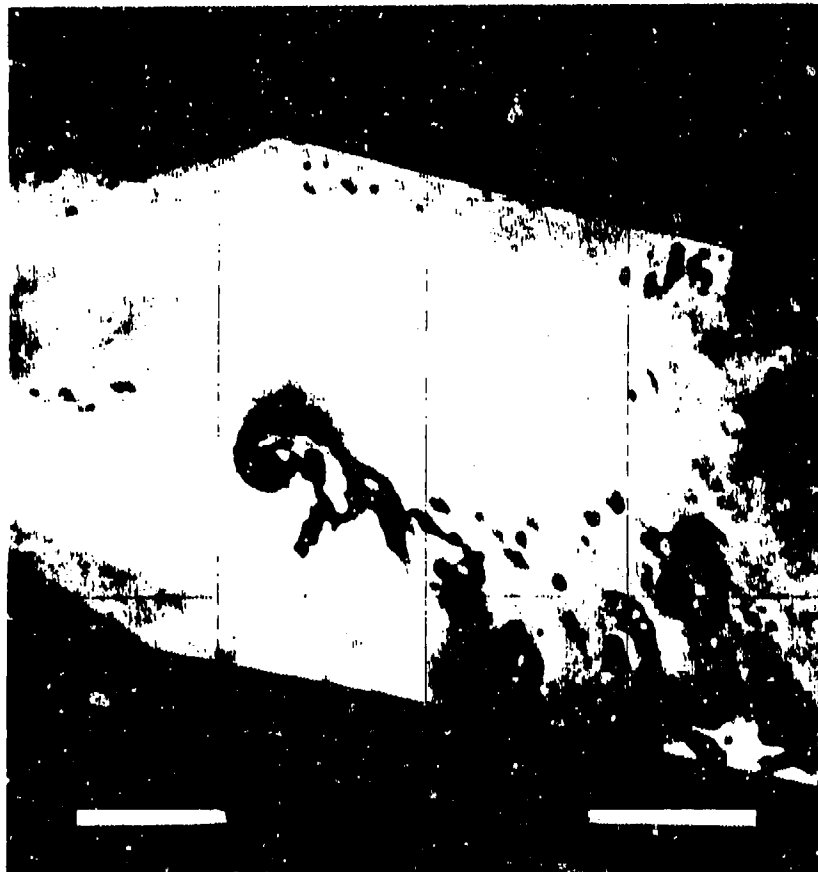


Fig. 47 — SSM/I 85H image of Typhoon Sperry

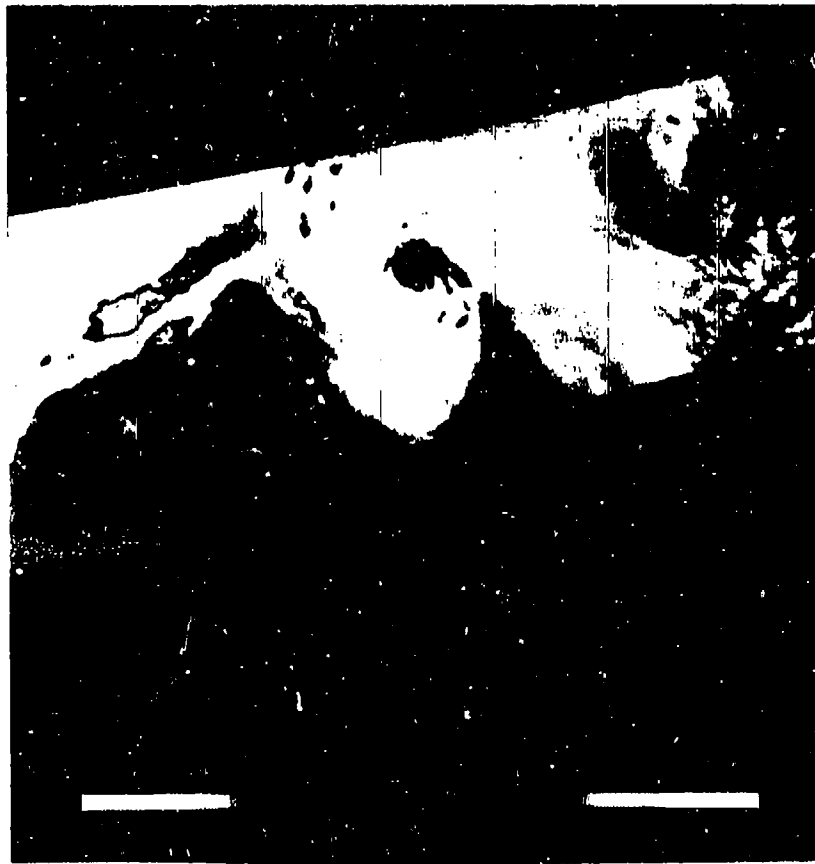


Fig. 48 — SSM/I image of clouds over eastern Pacific Ocean

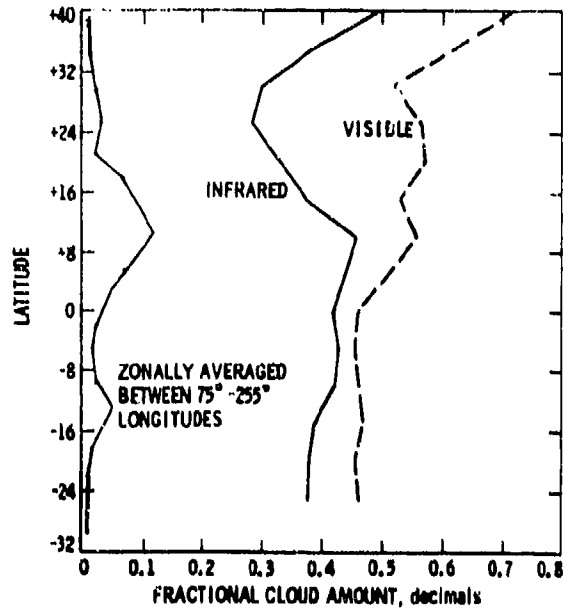


Fig. 49 -- Latitudinal coverage of clouds observed with the SSM/I



Fig. 50 -- SSM/I global product: cloud liquid water

graphed visual and IR data [8] for comparison. The color bar for Fig. 50 ranges from 0 to 1 kg/m<sup>2</sup> in units of 0.1. The purple regions are associated primarily with transmissive cumulus and cumulostratus clouds. The maximum values in the coverage plotted between latitudes 8 and 20 deg were associated with the deeply convective regions of the Intertropical Convergence Zone (ITCZ). The coverage of microwave clouds was less than 10% for these latitudes and nearly zero at higher latitudes where the atmosphere was nearly transparent all the time except for occasional thunderstorm activity. In contrast, visual clouds hid the surface approximately 50% of the time at equatorial latitudes and covered progressively more surface more of the time toward higher latitudes. Also in contrast to the visual case, those clouds nearly opaque in microwaves were deeply convective storms and highly transient locally. They are short-lived compared to visual cloud cover. A nearly opaque microwave cloud usually advects across the surface at 20 km/h or faster, so that it would cross a 400-m footprint of the sensor in about 1 min., leaving the atmosphere clear again. On the other hand, the microwave capability of sharply imaging these deeply convective clouds at higher resolution also would provide us opportunities to analyze certain highly important climatic processes associated with global circulation.

The global circulation system and the hydrological cycle, and certain large-scale weather patterns, such as tropical storms and the El Nino-Southern Oscillation (ENSO), depend on small-scale convective processes in the atmosphere. These small-scale energy processes, on scales of a few hundred meters to a few kilometers, are not all well-resolved with current visual, IR, and passive microwave remote sensors, such as AVHRR, OLS, GOES, and SSM/I. Water vapor, cloud liquid water, and rain typically tend toward maxima in the equatorial regions where solar heating is greatest. For example, two-thirds of global precipitation (global average, 1 m) falls in the tropics and subtropics. The condensation of water vapor to cloud liquid water and rain releases heat inside the atmosphere, which forces global-scale motions in the troposphere. The nature of this heat release, coupled with the resulting motions, concentrates the tropical rainfall into a latitudinally thin region called the Intertropical Convergence Zone (ITCZ). Within the ITCZ, at a given time, the rain may fall from roughly 30 individual cloud clusters, as in Fig. 50, each several hundred kilometers across [8]. Within these cloud clusters, vertical energy transports and about 60% of the rainfall are further concentrated into approximately 2,000 towering cumulonimbus clouds called "hot towers." These carry high-energy air up to the upper troposphere, a function essential in driving the world-wide meridional circulation called the Hadley cell [9,10]. Field studies have shown that these towers contain updrafts ranging from about 5 to more than 30 m/s and sometimes generate rain rates well above 100 mm/h over areas 4 × 4 km or smaller [11]. The remainder of the rain falls at much more gradual rates, < 10 mm/h, from the large "anvils" or stratiform extrusions from the hot towers. The number, size, and preferred location of these cloud clusters vary considerably, on time scales ranging from days to years or longer, so that the atmospheric heat engine has a variable output [12-20]. A large body of observational and modeling evidence implies that year-to-year variability of the latent heat released by the cloud clusters is a leading cause for short-term global climate variations, such as the El Nino-Southern Oscillation [21]. In certain favored locations also, about 1 in 10 cloud clusters may deepen into a tropical cyclone [8], such as the one in Fig. 47. The tropical cyclone, in other words, probably includes a high-density aggregate of larger than the usual number of hot towers for a cloud cluster. The exact mechanisms of cyclogenesis for the tropical and for the smaller arctic cyclones are not known but are believed to be involved with the smaller-scale, 300 m or less, energy processes associated with these convective columns and their environment.

An advantage of high-resolution visual and IR sensors is that they can provide information on cloud patterns, temperatures, and radiance at, primarily, the upper and middle levels of the atmosphere. The great advantage of passive microwave sensors is *that they can* provide information on all levels of the atmosphere, especially the lower level and the surface, in all weather, day or night. Passive microwave sensing is ideal for imaging the geometry and microphysical processes of atmospheric features, including

the convective regions. The observations of deeply convective regions is only an obvious example of the capability of 90 GHz microwave imagers to detect atmospheric features. Likewise, the microwave signal for at least each feature of Tables 4 and 5, including other types of clouds, is resolved according to its own emission and extinction characteristics and patterns of brightness.

The discussion of clouds, so far, has pertained to their properties of radiative extinction. In addition to affecting the radiation from below, clouds are fairly good emitters. Like extinction, the emissivity of a cloud depends on its thickness and water content. The scattering of microwaves by water droplets, within thin nonprecipitating clouds less than about 2-km vertical thickness, tends to brighten the cloud above background as shown in model calculations in Fig. 51 [22]. As the vertical thickness of the cloud increases beyond about 2 km however, the attenuation by absorption begins to dominate, and the cloud begins to darken relative to background. Nonprecipitating clouds, therefore, can have a range of emissivities  $\leq 0.9$ . As the cloud begins to precipitate, the attenuation of microwave transmission increases dramatically from approximately 1.0 dB at 0.5 mm/h to, for example 6 dB at 10 mm/h and 10 dB at 20 mm/h. As hail, graupel, and other opaque scattering material is added to the precipitating cloud in stormy systems, the attenuation can decrease the cloud's emissivity to 0.2 or less, depending on the type of atmospheric feature. The microwave signal, therefore, indicates the thickness and type of cloud; the pattern of emissivities of the cloud, and of local water vapor structure and windstreaming, all observed in the same imagery, indicates the type of atmospheric feature. For example, fronts are delineated by a line of high contrast in emissivity, usually enhanced by a wave of increased water vapor content, as in Fig. 37. Squall lines are fronts accompanied by increased windspeed and frequently followed immediately by deep convective clouds, as seen over Florida in Fig. 37. Squall lines, tornadoes, and tropical storms are sites of damaging convergent winds. Note the convergence of the windstreams in the southeastern part of Fig. 47. These features are complex, on scales smaller than the resolution of the SSM/I; with higher resolution, they can be precisely located and movement tracked. Upper atmospheric disturbances, such as atmospheric jets involved with cyclogenesis can be identified, as well as local turbulence with dimensions approaching 100 m as found near airports. Oceanic turbulence could be studied over large areas with 40 to 160 times the resolution presently available. In addition to studies of

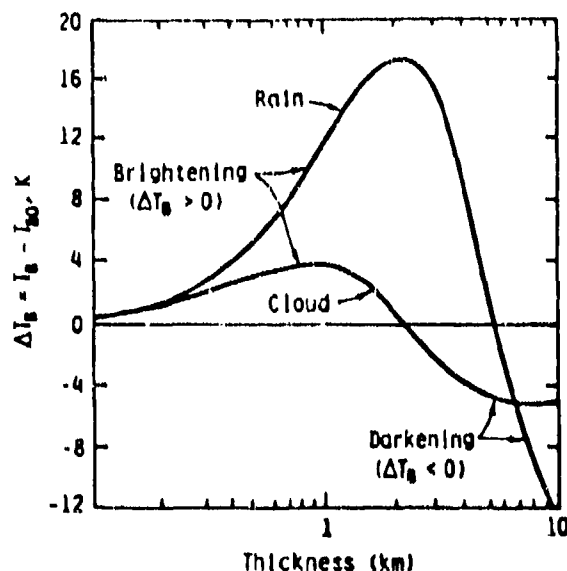


Fig. 51 --- Brightness variations of clouds and rain

free convective motions, forced convective motions such as orographic lifting, frontal lifting, gravity-wave displacements, and vertical motion induced by horizontal convergence of wind field could be analyzed on small scales. All of these mechanisms can produce an array of cloud types and species that can be identified at 90 GHz and analyzed for background clutter or other purposes.

### Aerosols and Particulates

Convective overturning to create clouds is not restricted to natural causes. Man-made features can create nonuniform local heating, as might be associated with induced thermals over parking lots or plowed fields, along highway systems or in a city's heat-island circulations. Observations on scales of hundreds of meters would be required for analyzing these effects. Industrial smokestacks, including those of ships, create clouds of pollutant aerosols and atmospheric wakes on scales of 100 m to about 10 km. Figure 52 is an example of atmospheric wakes at 1-km resolution, with anomalous cloud lines produced by ships under an SSM/I overpass. As observed, this phenomenon is on the edge of detectability with the current SSM/I resolution of 13 km, but the capability to detect and track atmospheric wakes on smaller scales has obvious importance in both naval surveillance and in studies of the effects of man-made aerosols on atmospheric integrity and climate. The baseline-system's resolution of 100 to 400 km is closely matched with the narrow dimension of the ship's atmospheric wakes, which grow from somewhat less than 1 km at formation to 10 or more km before they dissipate. Contrasts of about 1 K have been measured at 85.5 GHz with the SSM/I, which indicate contrasts of a few or more degrees with the baseline system and are, therefore, easily detectable.

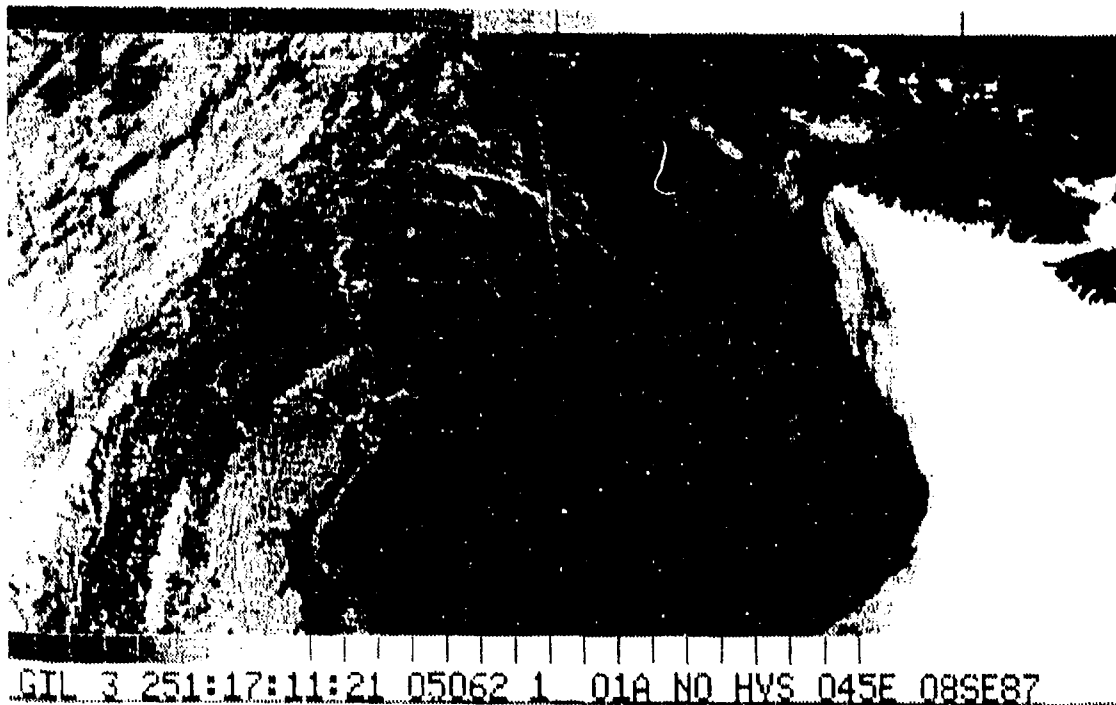


Fig. 52 — AVHRR visual image of atmospheric ship wakes

The precise physics of anomalous cloud lines is not yet clear, and the universality or frequency of occurrence is not yet defined. Smaller scaled observations are needed. Current observations indicate that, at least, the phenomenon occurs when vessels move under a fairly calm atmosphere, and microscopic particulates from the ship's exhaust stacks rise into the middle atmosphere. The particles become nuclei around which water vapor condenses. Although the condensation occurs regardless of winds, calm air preserves the trail long enough to give the impression of an ocean with numerous ships. The particulates absorb sunlight and add to atmospheric heating. At the same time, the droplets that form around the particles reflect sunlight back into space. The resultant effect may be very important in the equation of long-term global energy balance.

Volcanos are a major natural source of atmospheric particulates that has a significant impact on climate. Figure 53 shows a GMS visual image of the eruption of Volcano Pinatubo during a typhoon. The 85H microwave image (Fig. 54) and the visual image show different patterns of the eruptive plume at different levels of the atmosphere. The deep blue pattern at the center of crosshairs in Fig. 54 identifies the larger ejecta within the dust plume seen in Fig. 53. The multisensory imagery will be useful in testing models for the constituency of volcanic particulate matter and its contribution to the various levels of the atmosphere. In addition, the microwave imagery is valuable because of its view through the upper levels of smaller-sized volcanic ash, as well as clouds, which are opaque to visible and IR radiation. The attenuation of microwave radiation at lower levels in the volcano is probably caused by backscattering from larger, hail-sized particles.

A second example of atmospheric particulates is caused by naturally occurring dust storms, as observed in Fig. 55. In this case, the particles are approximately 50 to 100  $\mu\text{m}$  in size, about the same as that for light rain-sized hydrometeors. It appears that the dust just begins to scatter measurably at 85.5 GHz, as observed in Fig. 56, but not enough to significantly degrade the microwave view through the dust. Technology base studies have shown that sufficient dust to severely attenuate near-IF and optical links does not significantly attenuate microwaves near this frequency [23]. The microwave image of the dusty atmosphere near the West African coast in Fig. 56 is colored turquoise; land has been saturated white. This SSM/I overpass follows the one for Fig. 36 by about 12 h.

A third example of atmospheric particulates is the oil fires created in the Persian Gulf War. Figure 57 is a visual image of the scene when atmospheric contamination by smoke was sufficient to make the atmosphere nearly opaque at optical and IF wavelengths. Figure 58 shows the corresponding 85.5 GHz image of the same scene at that time. Dense smoke of this kind is transparent to microwaves.

### Operation Desert Storm

The final image (Fig. 59) illustrates one contribution that SSM/I microwave imagery provided in Operation Desert Storm. Daily SSM/I briefings were given to the Pentagon by NPOC and AFGWC, with NRL consultation, during Operation Desert Storm, and DMSP (Defence Meteorological Satellite Program) SSM/I and OLS imagery were dispatched regularly to the Middle East operations area. The first three images in the mosaic are examples of the kind of imagery that was used in operations planning, and the fourth image is an example of what could happen if SSM/I imagery were not used. The case was made, and a final report by the SSM/I Special Projects Office (SPO) was that the use of SSM/I and OLS imagery shortened the final phase of the war by about 10% (4 days).

The upper left image in Fig. 59 is infrared data from the OLS sensor aboard the DMSP-F8. OLS visible imagery was used also. This imagery shows the kind and extent of cloud cover over the area. The

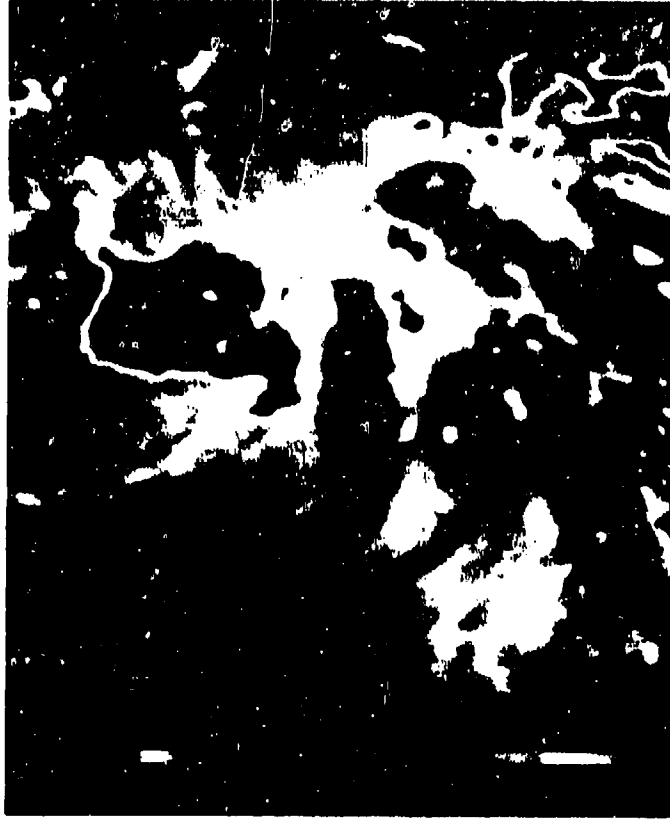


Fig. 54 — SSM/I 85H image of Volcano Pinatubo

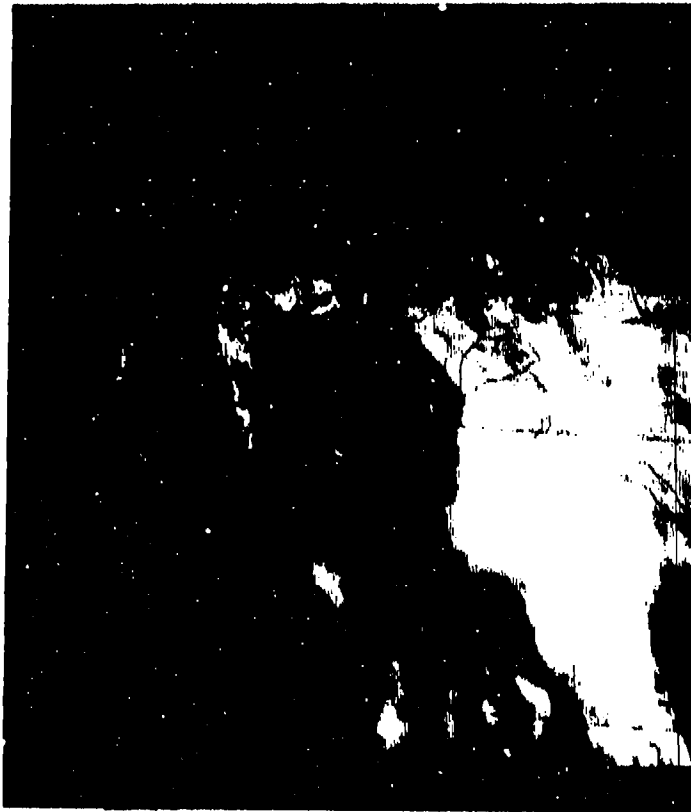


Fig. 53 — GMS visual image of Volcano Pinatubo

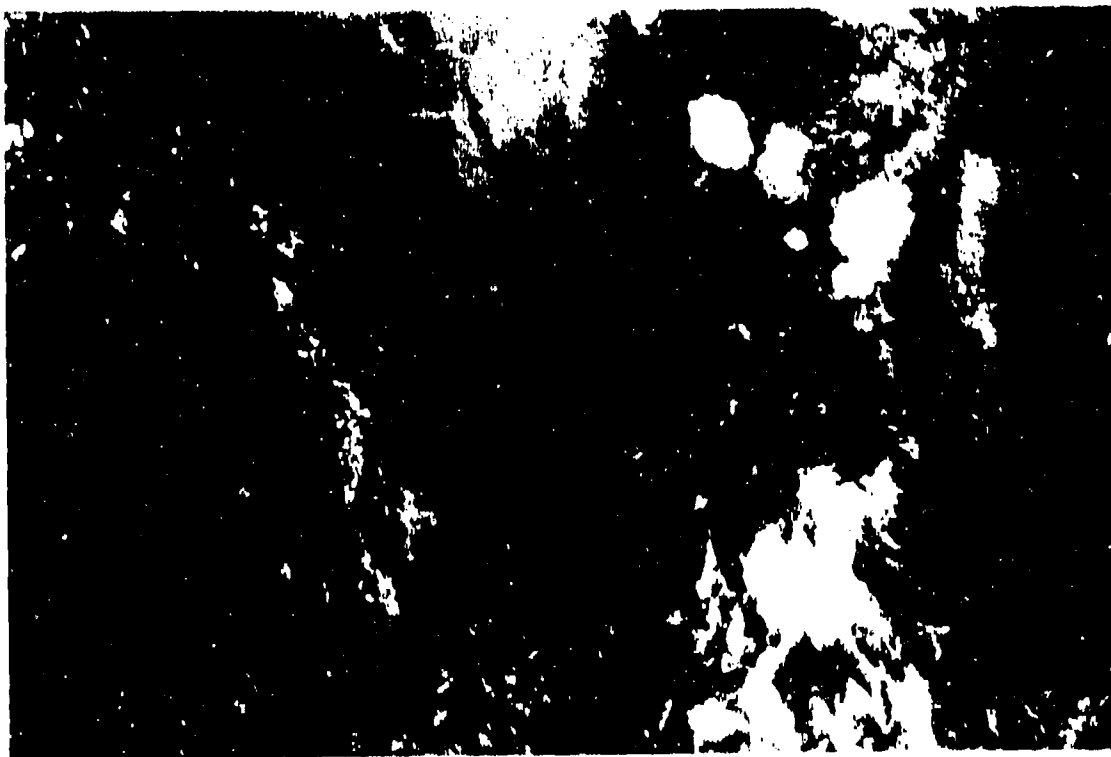


Fig. 55 — OLS visual image of an African sandstorm

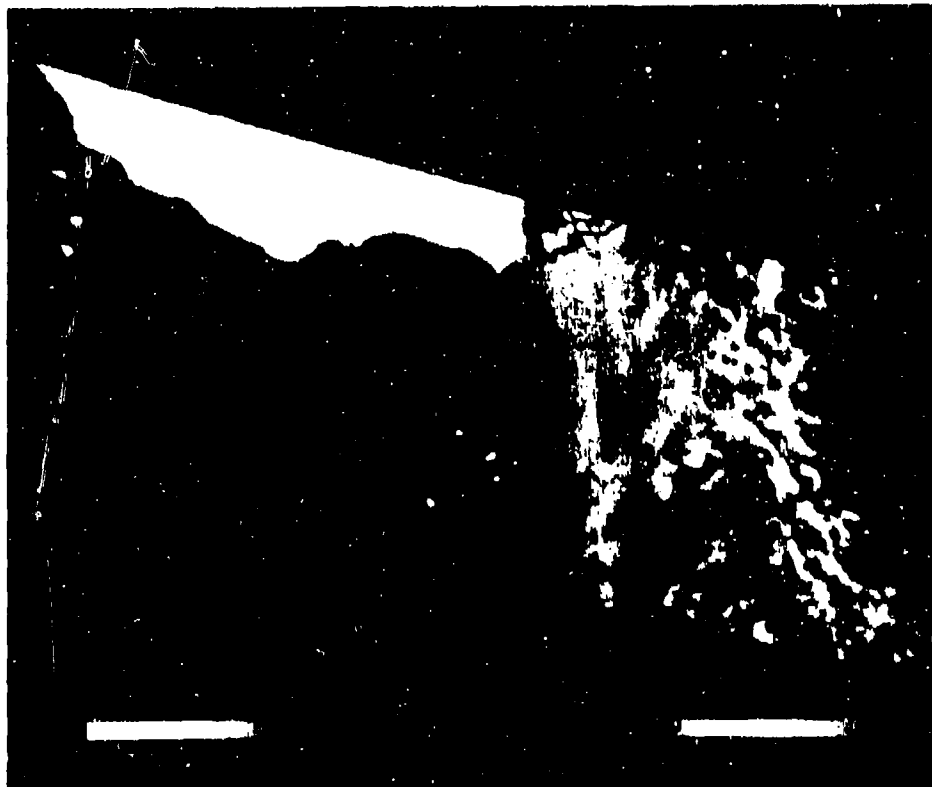


Fig. 56 — SSM/I 85H image of an African sandstorm

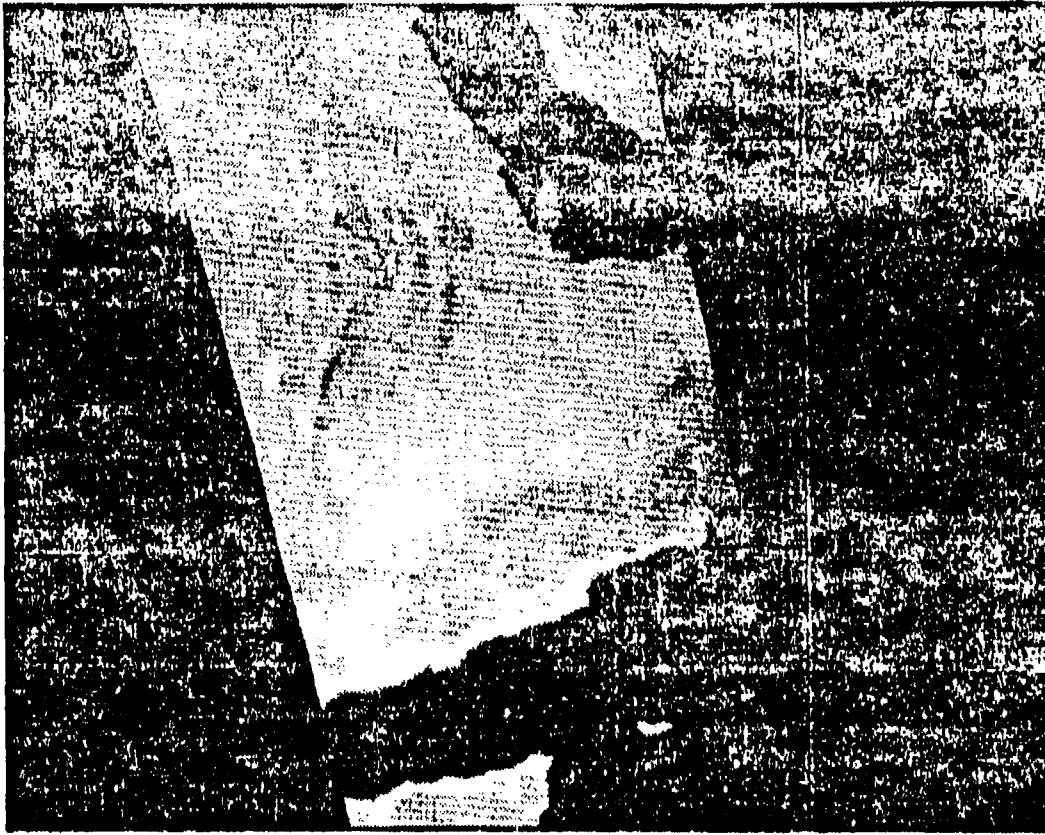


Fig. 58 — SSM/1 85H view through smoke over Kuwait



Fig. 57 — AVHRR visual view of smoke over Kuwait



Fig. 59 — SSM/I contribution to Operation Desert Storm

lower left image is SSM/I 85.5 GHz data from the F-8 bird. It shows, at maximum current resolution and sensitivity, the intensely convective regions where rain and possibly high wind could be expected. The upper right image is a combination of channels of the SSM/I that are suitable for depicting, not only the signal of conditions for thunderstorm activity, but also the areas of heavy ground water or mud resulting from heavy rains.

## SUMMARY

A series of SSM/I multichannel microwave radiometric systems aboard the Defence Meteorological Satellite Program (DMSP) have demonstrated the value of millimeter-wave radiometry from space for environmental measurements. The SSM/I operates at frequencies between 19 and 85 GHz, with surface resolutions ranging from 70 to 13 km. It obtains synoptic maps of critical atmospheric, oceanographic, and land parameters on a global scale. In particular, it quantifies the presence of water vapor, cloud water, and precipitation and locates and defines the structure of squall lines, hurricanes, weather fronts, clouds, and convective regions. It measures marine wind speed, locates the sea ice edge, and determines sea ice concentration and age. It is able to identify 14 different land surface types including snow cover, vegetation cover, arable soil, desert, and various stages of soil moisture.

The baseline system described in this report, with a surface resolution of 100 m, would define similar environmental structure but with a hundredfold increase in resolution. It could provide detailed information on water/land boundaries, wetlands, drainage patterns, cultivation, vegetation, volcanoes, storm damage, and snow cover. It would allow location of polyenas, leads, and sea ice concentration for greatly improved navigability through sea ice. It would be able to accurately locate the eye and structure of hurricanes, convective regions, and storms. It would be able to quantify oil spills, track their motion and allow more efficient and effective containment and clean up. It would be able to locate the burning regions and extent of forest fires through the smoke to assist firefighting efforts.

Furthermore, the baseline system would be able to provide information on a wide range of man-made structures with equal day and night sensitivities and on a near-all-weather basis. It could detect single Backfire bombers and ships the size of attack boats as well as flights of smaller aircraft and concentrations of 20 or more tanks or vehicles. It could define trains, terminals, rail networks, bridges, roads, runways, airports, large buildings, oil storage tanks, and residential and industrial areas. It could provide battlefield damage assessment through smoke, haze, and dust. This system would provide a more-than hundred fold increase in surface resolution from space. It would provide capabilities much, much greater than any existing system. As such, it would undoubtedly result in new applications, uses, and benefits beyond those detailed above and not easily predicted.

## REFERENCES

1. L.R. Gaddis, P.J. Mougini-Mark, R.B. Singer, and V. Kaupp, *Geol. Soc. Amer. Bull.* 101, 317 (1989).
2. D.R. Brunfeldt and F.T. Ulaby, *IEEE Trans. Geosci. Remote Sensing GE-22*, 520-524 (1984).
3. E. Schanda, C. Maetzler, and K. Koenzi, *Int. J. Remote Sensing* 4, 149-158 (1983).
4. B.E. Troy, J.P. Hollinger, R.M. Lerner, and Wisler, *J. Geophys. Res.* 86, 4283-4289 (1981).

5. J.P. Hollinger, B.E. Troy, Jr., R.O. Ramseier, K.W. Asmus, M.F. Hartman, and C.A. Luther, *J. Geophys. Res.* **89**, 8104-8122 (1984).
6. A. Mugnai, H.J. Cooper, E.A. Smith, and G.J. Tripoli, *Bull. Amer. Meteor. Soc.* **71**, 2-13 (1990).
7. E.M. Agee and T. Assai, eds., *Cloud Dynamics* (Kluwer Academic Publishers, 1982) pp. 57-71.
8. R.H. Simpson and H. Riehl, *The Hurricane and Its Impact* (Louisiana State University Press, Baton Rouge and London, 1981) 398 pp.
9. H. Riehl and J. Simpson, *Phys.* **52**, 287-304 (1979).
10. D.P. Jorgensen, *J. Atmos. Sci.* **41**, 1268-1285 (1984).
11. R.A. Houze, Jr., 1982, *J. Meteor. Soc. Japan* **60**, 396-410 (1982).
12. J. Bjerknes, *Mon. Wea. Rev.* **97**, 163-172 (1969).
13. J.D. Horel and J.M. Wallace, *Mon. Wea. Rev.* **109**, 813-829 (1981).
14. P.J. Webster, *J. Atmos. Sci.* **38**, 554-571 (1981).
15. P.J. Webster, *J. Atmos. Sci.* **39**, 29-40 (1982).
16. K.M. Lau and P.H. Chan, *Mon. Wea. Rev.* **113**, 1889-1909 (1985).
17. K.M. Lau and P.H. Chan, *Bull. Amer. Meteor. Soc.* **67**, 533-534 (1986).
18. K.M. Lau and P.H. Chan, 1987, *J. Atmos. Sci.* (1987).
19. A.C. Lorenc, *Quart. J. Roy. Meteor. Soc.* **110**, 427-441 (1984).
20. K.M. Weickmann, G.R. Lussky, and J.E. Kutzbach, 1985, *Mon. Wea. Rev.* **113**, 941-961 (1985).
21. E.M. Rasmussen, *Amer. Scientist* **73**, 168-178 (1985).
22. L. Tsang, J.A. Kong, E. Njoku, D.H. Staelin, and J.W. Waters, *IEEE Trans. Antennas Propag.* **AP-25**, 650-651 (1977).
23. D.G. Bauer, R.A. McGee, J.E. Know, and H.B. Wallace, Ballistic Research Laboratories, Memo #53 (1977).